Finite Element Based Micromechanical Modeling of Periodic Composite Microstructures

by

Matthew J. Rosario

SUBMITTED TO THE DEPARTMENT OF MECHANICAL ENGINEERING IN PARTIAL FULFILLMENT OF THE REQUIREMENTS FOR THE DEGREE OF

BACHELOR OF SCIENCE IN MECHANICAL ENGINEERING

AT THE

MASSACHUSETTS INSTITUTE OF TECHNOLOGY

JUNE 2010

Signature of Author: _____
Department of Mechanical Engineering
May 17, 2010

Certified by: _____
Mary C. Boyce
Gail E. Kendall Professor of Mechanical Engineering
Head of Department
Thesis Supervisor

Accepted by: _____
John H. Lienhard V
Collins Professor of Mechanical Engineering
Chairman, Undergraduate Thesis Committee

Finite Element Based Micromechanical Modeling of Periodic Composite Microstructures

by

Matthew J. Rosario

Submitted to the Department of Mechanical Engineering
On May 17, 2010 in Partial Fulfillment of the
Requirements for the Degree of
Bachelor of Science in Mechanical Engineering

ABSTRACT

The mechanical behavior of cellular solids, including stiffness and strength, can be tuned by tailoring the underlying geometry and material constituents of the microstructure. Here the effect of key parameters on the compressive deformation response of composite truss-based cellular solids was investigated. A simple periodic geometry was chosen and studied using finite element based micromechanical models. Simulations were conducted parametrically varying the volume fraction with a fixed strut length, the proportion of the polymer coating to the elastomer core used in the composite struts (coating fraction), and the size of the representative volume element (layer number). An analytical model based on energy methods for buckling columns with elastic restraints was also derived and compared to the simulation data. Materials were then fabricated using 3D printing and then tested in compression. Numerical and experimental results are compared.

The simulations showed that an increase in volume fraction with coating fraction and layer number held constant increased the modulus in a linear manner, and increased the peak stress with a non-linear dependence. An increase in coating fraction with volume fraction and layer number held constant significantly increased the modulus as the square of the volume fraction and the peak stress in a non-linear fashion. An increase in the layer number lowered the critical buckling strength of the geometry non-linearly, the trend verging asymptotically with increasing size and depending heavily on the effective buckling length of the structures.

The experimental modulus agreed well with the simulated data for the polymer and elastomer samples, and the experimental peak stress was found to be a lower value than predicted, due mainly to imperfections in the struts. There was a disparity between experimentation and simulation for both the modulus and the peak stress of the composites. One potential cause for this is the non-uniformity of the 3D printed coating, which was examined microscopically and found to have many imperfections along the polymer coating. Off-axis loading of the samples was also determined as a cause. Future work depends on advances in the resolution and repeatability of 3D printing technology.

Thesis Supervisor: Mary C. Boyce

Title: Gail E. Kendall Professor of Mechanical Engineering, Head of Department

Table of Contents

List of Figures

List of Tables

Acknowledgements

The author would like to graciously offer thanks to Professor Mary C. Boyce for the suggestion of the topic and invaluable input and comments along the way. Without her expertise and vast array of knowledge in mechanics and materials this research would not have been possible.

In addition, many thanks are due to Dr. Lifeng Wang for serving as a mentor and a partner in this research; his contributions are too large and too numerous to be listed here.

The author would also like to acknowledge the Institute for Soldier Nanotechnologies for support in the early stages of this research and also for the use of the extensive facilities at the Technology Square campus, and the Department of Mechanical Engineering for the use of additional resources for experimental testing and simulation.

Chapter One: Introduction

Recent advances in materials technology allow for the design and fabrication of micro- and nano-scaled structures to serve as cellular units in macro-scale materials. Because the properties of these structures are governed by the principles of cellular solids, they allow for a wide range of variability in mechanical properties. Open-cellular materials with a structured architecture in particular allow for an extensive range of property tuning based on characteristics intrinsic to the foam. For example, adjusting the volume fraction of a foam can allow a material to display a wide range of stiffnesses, with an upper bound of the stiffness of the solid. Periodic truss-based cellular solids are a prime example of such structures.

Foams appear regularly in nature, and frequently in the most demanding structural applications. Wood, cork, and cancellous bone, and coral are all significant examples of natural foams that can endure high static and significant repeated loading [1]. In the modern age of manufacturing, composite materials are also in demand for applications where high strength with low weight is crucial; one can see these materials everywhere from the plywood in a house to the carbon fiber on the wing of a fighter plane.

While changes to the geometry can drastically affect the properties of the foam, added variability can be achieved through subtler touches to its composition. Instead of periodic single-material foams, composite trusses allow for a novel mechanical response. A composite truss comprised of an elastomer coated with a glassy polymer can exhibit high stiffness and strength during the initial stages of compressive loading, and significant energy dissipation after the yielding of the column. Such structures would become materials with a combination of high stiffness and high strength together with low weight, and possibly energy absorption or dissipation.

The applications for this research are significant and diverse. Apart from a drastic reduction of weight and material to achieve a similar macroscopic performance, the energy dissipative characteristic of the foam appeals to high-rate impact applications in personal protection, as well as low-rate impact applications such as device packaging. The particular combination of materials here is also extremely temperature dependent, and as such can respond as a tunable microstructure with thermal input. A further application of that concept leads to "soft robotics," whereby robotic structures (or any structures) can dynamically change stiffness through thermal activation, transforming a rigid joint to a compliant one and vice versa [2].

This thesis is an attempt to systematically study the effects of periodic composite truss microstructures and the effect of a number of microscale geometric parameters on the macro-scale behavior of the material. To that effect, a general finite-element simulation of a particular periodic microframe structure was developed. An algorithm was constructed to apply periodic boundary conditions to the cubic geometries of the repeating elements simulated. The parameters varied were the volume fraction of the material; the strut composition, which included a solid core with an outer coating; and the number of layers incorporated into a representative volume element. These finite-element simulations were verified through the development of an analytical model to predict quantities of interest – the modulus of the cellular solid and critical buckling stress. The simulations and calculations were also verified through the fabrication and subsequent compression testing of physical samples of the geometry.

This thesis is structured to first introduce theory, followed by modeling, followed by experimental results and conclusions. Chapter Two introduces the analytical model for stiffness and compressive strength of the cellular solid. Chapter Three covers the finite-element based

micromechanical modeling of the microstructure, including the model, the procedure, and results. Chapter 4 reviews the conducted experiments and validation of the finite-element model. Finally, Chapter 5 offers conclusions and suggestions for further work on the topic.

Chapter Two: Analytical Model of Stiffness and Strength of Periodic Cubic Cellular Solids

2.1. Stiffness

A prominent characteristic of a foam is the volume fraction V_f. This property, also known as the relative density [3], indicates the amount of total volume in a foam is occupied by the solid material. Though some extremely low-density foams can reach volume fractions as small as 0.001, the range for most practical applications is 0.05 to 0.30. Above $V_f = 0.30$, the mechanics of the foam respond more like a solid material with isolated pores than as a cellular solid structure [4]. The foam modulus, as it varies with the volume fraction, is the concern of this subsection.

As the mechanical properties of foams are an extension of the properties of the solid, foams drastically increase the range of these properties. The elastic modulus of foams typically ranges from 1MPa to 1 GPa, and can be as low as 1KPa. Most polymeric foams possess moduli within the 1MPa range; the elastomeric foams extend into the 10 KPa range. The combination of these two materials into a composite structure will have a resulting modulus within the bounds of each limit. The strength of foams exhibits a similar trend, typically extending from values of 10 MPa towards 10KPa [5].

The structure of a cellular solid can be classified according to a number of parameters, upon which its performance strongly depends. These are the volume fraction, the nature of its cells (open or closed), the material of which it is constructed, the mean cell diameter, and the particular cell geometry. Here we focus on open-cellular composite periodic structures with a cubic lattice structure, and as such, the materials and cell diameter are fixed features.

In an open-cellular foam, the cellular units are apparent from the edge geometry, but there are no faces to isolate each cell from another. As one might suspect, this significantly affects the performance of the material. The volume fraction of a foam scales directly with the square of the thickness-length ratio for open cells with an empirical constant in front which depends on the particular cellular geometry [6]. The form is shown in Eq. 1:

$$V_f = C\left(\frac{s}{l}\right)^2 \tag{1}$$

where s is the strut width, l is the strut length, and C is an empirical constant, with $C = 3$ for this geometry.

A dimensioned drawing of the specific geometry used in this study is provided in Figure 1, including variables that will be referenced throughout the thesis. The truss width s is the side width of the square column. The coating thickness t is the width of the outer layer of coating. For this study, the strut length l is fixed at a rigid value of 7 mm, regardless of the volume fraction.

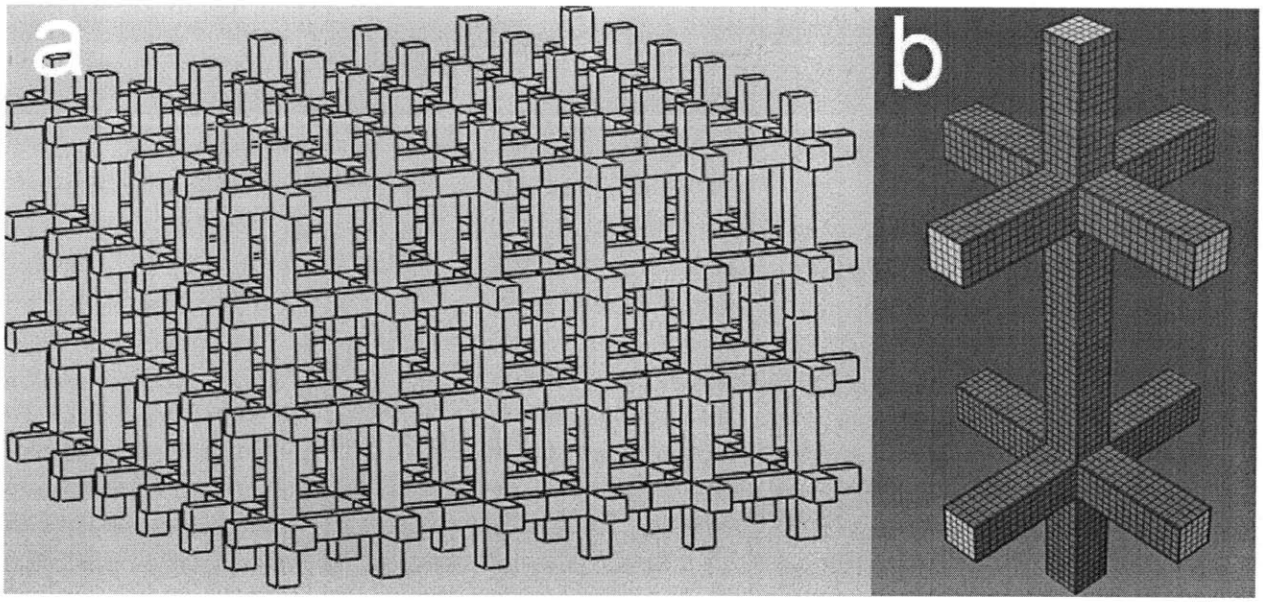

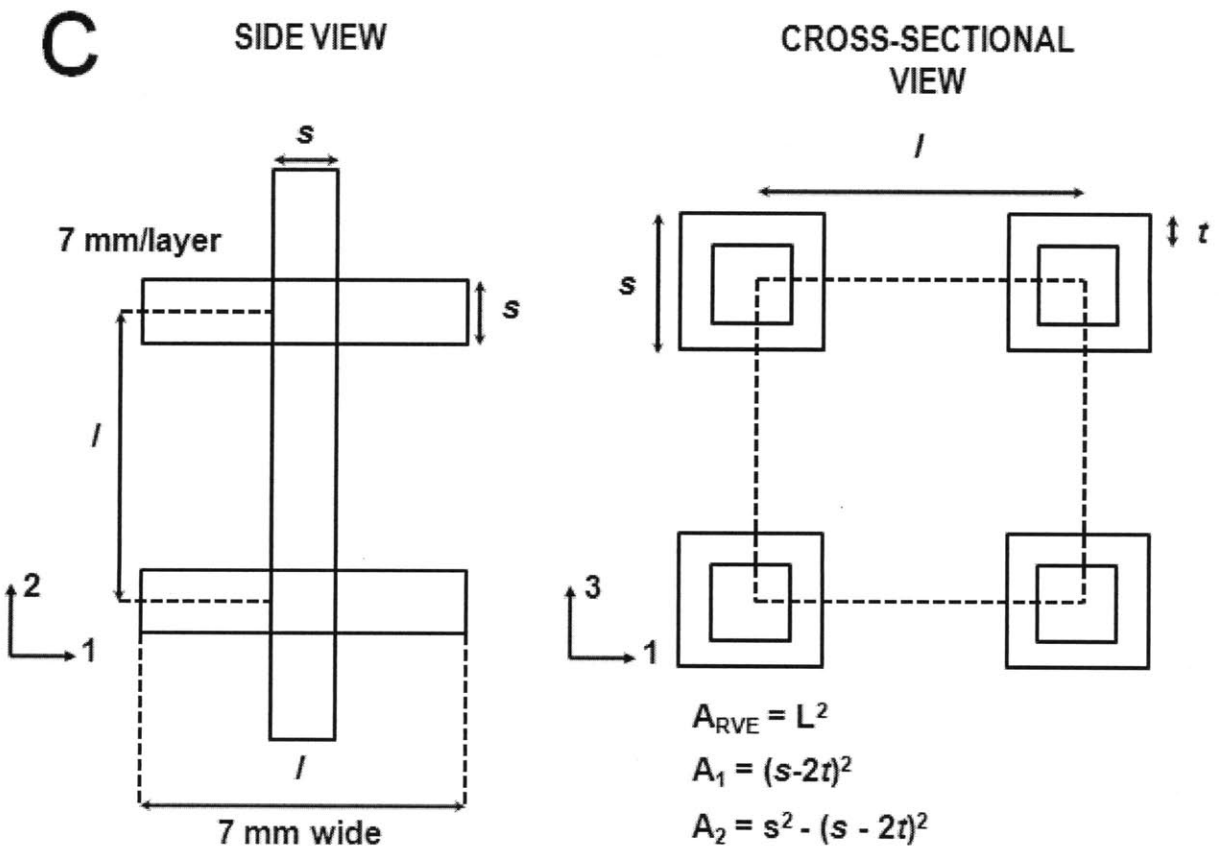

Figure 1: Geometry of the truss-based structures considered here. a) 3D geometry of the full structure. b) A fully meshed representative volume element (RVE) comprised of finite-elements. c) A 2D schematic of the RVE geometry, including variables.

The compressive loading of the columns of the microstructure forms the crux of this thesis, and as such it is important to investigate the deformation mechanisms resulting from it.

The first manner of deformation the truss will undergo is a pure axial compression. The mechanics of axial loading of a column is straightforward. The deformation is related to the loading force through the axial stiffness of the column by

$$\delta = F\frac{L}{EA} \tag{2}$$

where L is the column length, A is the cross-sectional area, and E is the elastic modulus [7].

For the uniform loading of composite columns, it is necessary to derive an effective modulus to simulate a material that would deform the same way as the composite. One can do this by taking the average modulus weighted by the areas of the two sections, resulting in

$$E = \frac{E_1A_1 + E_2A_2}{A_{RVE}} \tag{3}$$

where E_1 and A_1 are the modulus and area of the first section, E_2 and A_2 are the modulus and area of the second section, and A_{RVE} is the area of the total representative volume element (RVE) (see Figure 1).

Of course, for the foam considered here, the total cross sectional area is not simply the area of the column, but the entire area of the RVE. This accounts for the open space surrounding the column, since only a fraction of our structure is solid. The elastic modulus is determined from the weighted average principle of Eq. 3. Calculated and simulated results were compared over a range of volume fractions (V_f=0.05, 0.10, and 0.20) and coating fractions (0%, 5%, 10%, 20%). An important note: the volume fractions referred to here and throughout the remainder of this thesis are rounded – the true volume fractions are 5.54%, 11.81%, and 19.83%, which are very close to the named values, but not exact. The coating fractions are exact values. All calculations use the exact values for each variable describing the structure.

If a column is initially tilted at a slight angle from the vertical, the initial modulus is significantly decreased. Instead of compression, the primary deformation mechanism is bending. The relation between the contact force and resulting deformation for a tilted column is approximated by [8]

$$P = \frac{\pi^2 EI}{4L^2}\left(1 - \frac{1}{\left(\frac{\delta}{L\tan^2\theta} + 1\right)^{1.15}}\right) \tag{4}$$

where EI is the bending stiffness, L is the column length, h is the deformation, and θ is the tilt angle. Because $E = \frac{d\sigma}{d\epsilon}$ at $\epsilon = 0$ and $\epsilon = \frac{\delta}{L}$, we can divide this force by the repeat area and take the derivative with respect to ϵ to find the effective modulus. The resulting expression is

$$E_{eff} = \frac{\pi^2 EI}{4L^2A_{RVE}}\left(\frac{1.15}{\tan^2\theta}\right) \tag{5}$$

The effect of bending via the angle dependence can drastically reduce the effective modulus of the column.

2.2 Compressive Strength Governed by Member Buckling

2.2.1 Buckling of a Column

Buckling is a mode of failure resulting from high compressive stresses. The onset of buckling occurs upon reaching a critical loading condition. Buckling is the predominant failure mode in long, slender columns, which lends it a particular relevance to this study.

While the compressive strength of a column is a material property, the critical buckling load of a column relies heavily on the geometry of the beam, the boundary conditions at the beam ends, and the nature of the loading condition.

For an ideal column loaded axially, the Euler buckling criterion relates the critical load to these properties by

$$P = \frac{n^2 \pi^2 EI}{L^2} \tag{6}$$

where EI is the bending stiffness, L is the length of the column, and n is a modifying constant that accounts for the boundary conditions imposed on the column [9]. This buckling equation can be adapted for many different geometries [10,11]. Though this equation assumes no eccentricity in the compressive load and neglects any lateral forces in the beam or imperfections in the geometry, it offers a good approximation of the buckling failure load for a slender column.

The effective length of a buckling column is governed by the boundary conditions on the column ends, which, in turn, governs the buckling mode. A column can be subjected to a variety of conditions at its ends, the most common of which can be found in Figure 2 with corresponding values of the constant n [12]. As can be seen, then, if both ends are fixed, the mode is constrained due to the rotational constraint at the boundaries; hence, the effective length of the column will decrease by a factor of two as compared to the case when both ends are pinned, which results in a critical buckling load four times greater. The higher buckling modes require significantly more energy, and for this reason structural buckling usually occurs at the lowest modes possible for the given boundary conditions. Figure 2 shows the lowest modes possible for each of the boundary conditions depicted.

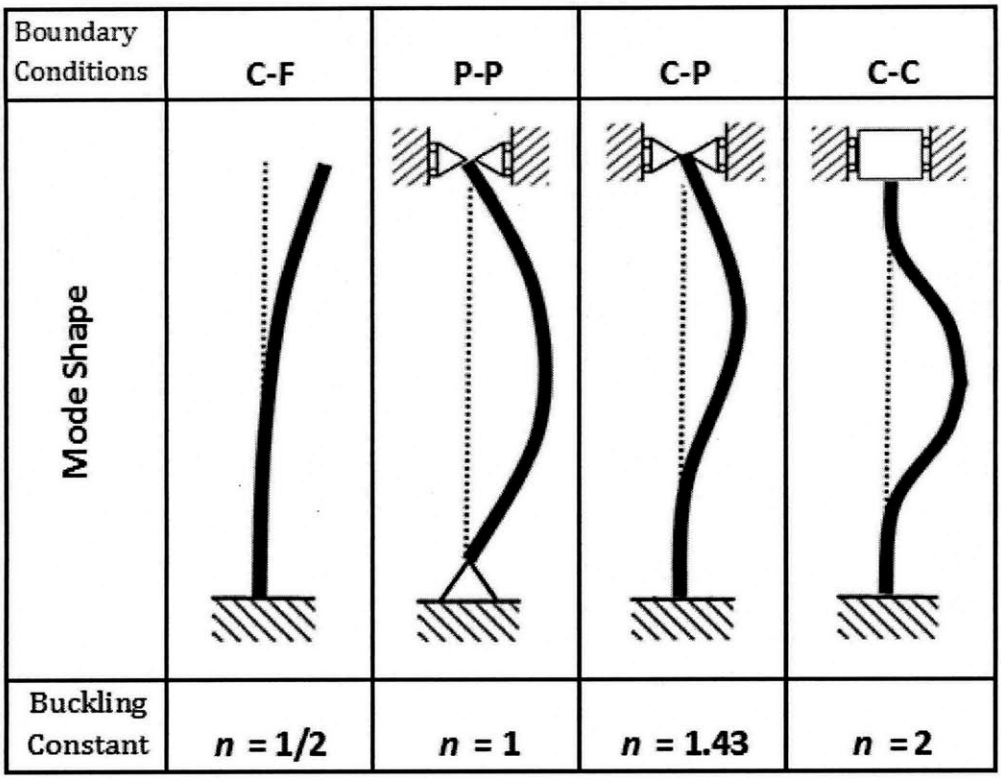

Figure 2: Mode shapes due to boundary constraints on bucking beams. The boundary conditions are, from left to right, Clamped-Free (C-F), Pinned-Pinned (P-P), Clamped-Pinned (C-P), Clamped-Clamped (C-C). Diagram adapted from *Buckling of Bars, Plates, and Shells* by Don O. Brush and Bo O. Almroth.

The critical buckling load of a composite structure can be calculated by determining the effective properties of the composite structure. In the case of the coated column, the effective bending stiffness *EI* is comprised of the sum of the individual bending stiffnesses of the two sections – namely

$$EI = E_1 I_1 + E_2 I_2 \tag{7}$$

The second moment of area must be calculated for each section and then multiplied by the corresponding elastic modulus. Of course, the buckling behavior on a column may occur about two orientations. The first is parallel to a given side of the square cross section of the column; the second runs along the diagonal from a given pair of corners of that cross section. Buckling will occur about the axis with the lowest *EI*.

Using the formula for the second moment of area of a square, we gain the second moment for the inner core, and we can subtract the inner area from the outer for the second moment of the coating, yielding the following two relations:

$$I_1 = \frac{(s - 2t)^4}{12} \tag{8}$$

$$I_2 = \frac{s^4 - (s - 2t)^4}{12} \tag{9}$$

Structural deformation is governed by one of several mode shapes based on the geometry of the deformed member. For the buckling of a column with pinned-pinned end conditions, the fundamental mode is expressed by the displacement equation of a half-sine wave [13]. This mode is fundamental because it is the natural "choice" for any slender column in buckling, since it requires the least energy (and therefore, the lightest load) to reach. In order for a column to buckle in any other mode, there must be a restraint on the system that augments the energy needed to reach the first mode. The second mode effectively halves the buckling length in Euler's equation, and because load scales with the square of the length, it requires four times more energy to reach the second mode when constraints are not present.

The utility of the composite column studied here depends very strongly on the materials of which it is comprised. A stiff interior column coated with a malleable material, i.e. rubber on steel, does little for the axial stiffness of the beam, since for any reasonable geometric ratio, the rubber provides negligible additional stiffness compared to the steel. If the materials were reversed, however, with a thin steel coating covering a flexible rubber core, the column properties become more complex. The value of critical buckling stress for the column would be dominated by the stiff outer ring.

The same principles hold true for a composite beam with a stiff polymeric outer coating and an elastomeric inner core. Once the polymer yields, the elastomer can still compress to extremely large strains, thereby absorbing high levels of energy while remaining fully reversible.

In order to establish the linear and nonlinear mechanical behaviors of these structures and composites, we consider the constituent material properties of a glassy polymer and an elastomer. Here the polymer is FullCure 720, and the elastomer Tango Plus. Both are commercial 3D printable materials from Objet Geometries Ltd. [14], and were selected so that experimental verification would be possible. The material properties for each were determined experimentally through uniaxial compression testing in a separate study [15], the results of which can be viewed in Figure 3. The Tango Plus sample was tested at a strain rate of 0.01 s^{-1}, and is fitted well by an Arruda-Boyce hyperelastic model with an initial modulus of 0.213 MPa and bulk modulus of 1 GPa. The FullCure 720 data was tested at three strain rates, 0.002, 0.01, and 0.05 s^{-1}. At a strain rate of 0.01 s^{-1}, the initial modulus was 1830 MPa, and the yield strength 75 MPa. The strain rate has a significant effect on the material response of this glassy polymer, and as such only those properties determined at a strain rate of 0.01 s^{-1} are considered for the simulation and experiments described here.

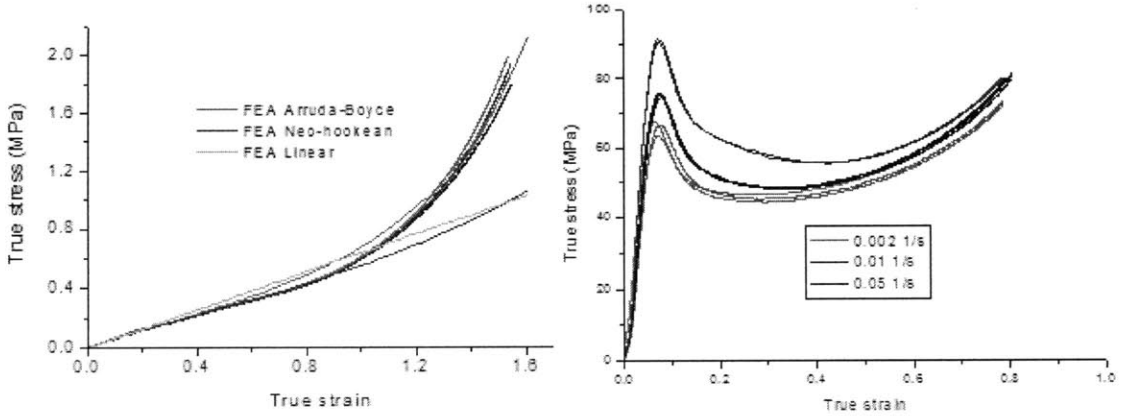

Figure 3: True stress-true strain curves for (a) Tango Plus in compression and (b) FullCure 720 in compression at three strain rates. Diagrams printed from an unpublished study "3D printing for porous structure and polymer composites" with permission from Dr. Lifeng Wang.

The behavior of any foam under compression can be dissected into three distinct realms [16]. The first is the linear-elastic regime, where the stress in the foam is directly proportional to the elastic strain. There is a collapse regime that follows, where the mechanism of deformation depends on the properties of the foam. For an elastomer, elastic buckling results in a sharp decrease in stiffness. For an elastic-plastic foam, the "yield" may be yielding of the polymer followed by plastic buckling. Finally, the third regime common to all foams is densification, where the foam, under high strain, begins to act as a solid and the stress rises steeply. See Figure 4 for examples of the compressive behavior for elastomeric and elastic-plastic foams.

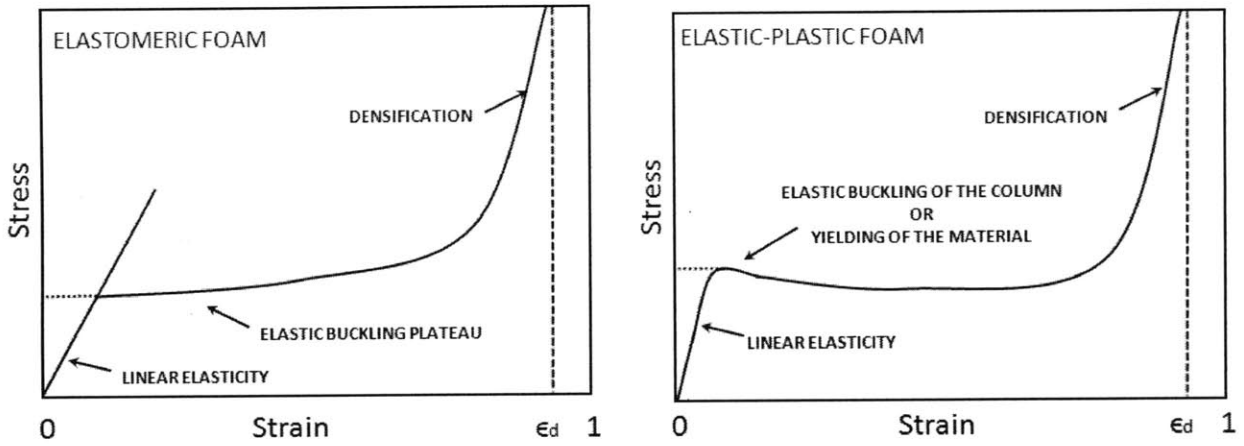

Figure 4: Stress-strain plots for elastomeric and elastic-plastic foams in compression, detailing the three regions of compressive strain. Diagram adapted from *Cellular Solids* by Lorna J. Gibson and Michael F. Ashby.

Our composite cellular solid exhibits the usual behavior in the linear-elastic regime, and we can model the transition to buckling from that initial stage. The polymer coating reaches the elastic-plastic transition after the structure buckles, and thus there is localized yielding that occurs at the strut-branch interface. Because the stiffness of the polymer is orders of magnitude above the stiffness of the elastomer, and the second moments of area are similar for both, the bending stiffness of the polymer is much greater than that of the elastomer. The deformation response is thus governed by the stiffer polymer at this critical point.

2.2.2. Influence of Lateral Constraints on Buckling

In determining the critical buckling stress, Euler's criterion is a useful starting point, but the buckling load for our columns is greatly influenced by the presence of support branches. It is not immediately clear what is the governing mode or buckling wavelength since the branches can influence the buckling mode. These branches can be approximated as elastic springs attached to a rigid boundary (see Figure 5).

These branches play a major role in the buckling of the structure; the buckling mode is not only affected by the spring forces that resist the lateral deformation of a column, but also by the location of the springs along the column. A stiff elastic spring at the midpoint of a column will be directly resisting the lateral displacement of first-mode buckling, and so influences the critical load far more than a spring located one-quarter of the total length from an edge of the column.

The periodic boundary conditions also dictate that the angle of the top surface of the column be identical to the angle of the bottom surface so that mating is possible: $\theta(0) =$

$\theta(L)$.This results in boundary constraints that not well-represented by analytical elements and not well-covered in the literature.

The combination of these elements and constraints are displayed in Figure 5. The complexities of dissecting this system analytically are not trivial, and are beyond the scope of this thesis. However, to verify that the RVE simulation is an appropriate tool for the simulation of our structures, this model was simplified and a trend determined to be compared to the finite element results.

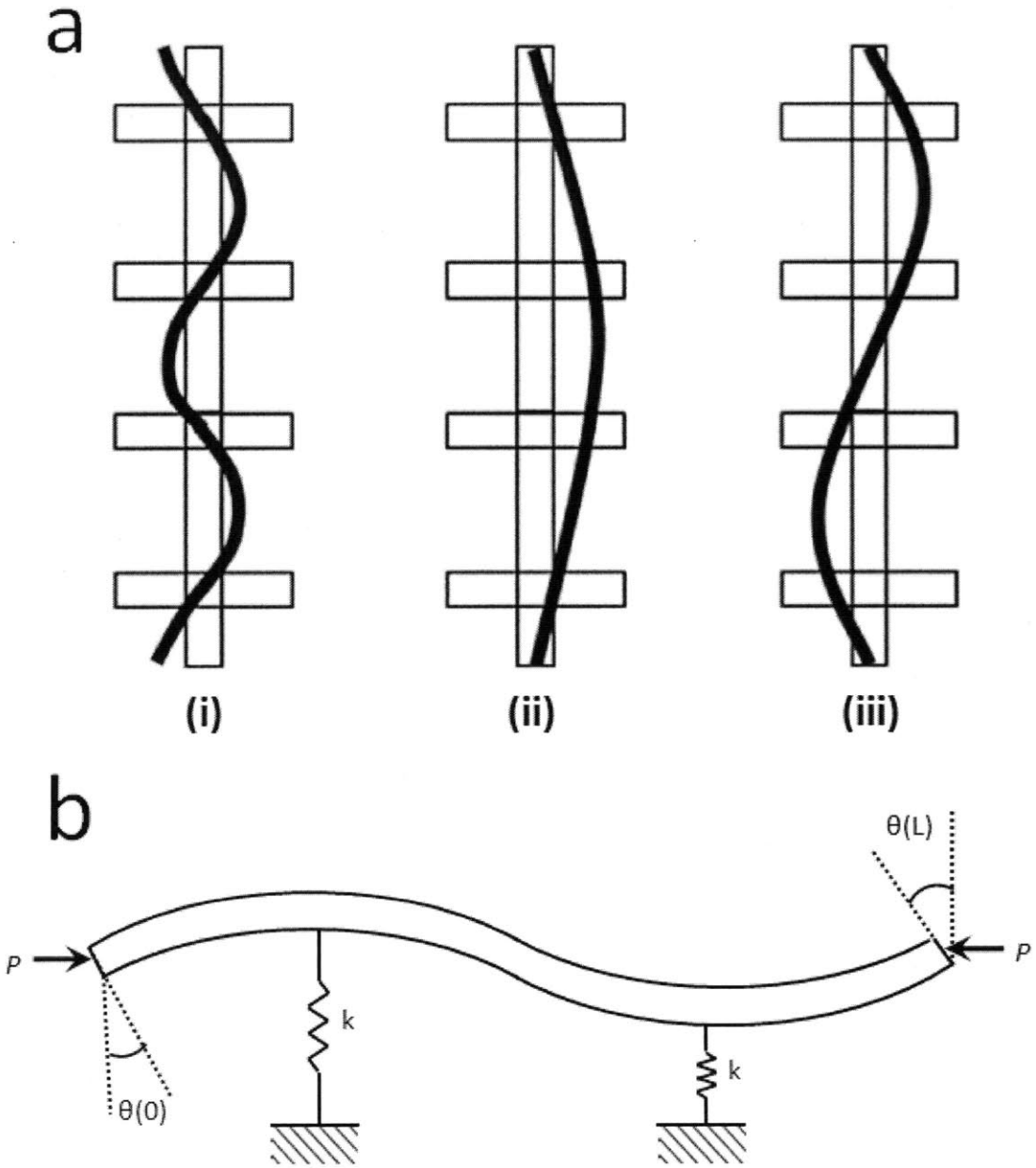

Figure 5: (a) The branches may act as a form of pinning point that constrains the buckling to the mode in (i), may not be influential at all (ii) or something in between (iii). (b) An approximate analytical representation of the buckling column for a two-layer RVE. Each branch supplies a lateral stiffness as well as an axial stiffness, and the periodic boundary conditions ensure that the column always deforms to the second mode.

The periodic boundary conditions at the ends of the column are not quite pinned supports, nor are they a rigid constraint. However, since the analytics become complex, we assume that the end conditions are similar enough to pinned supports and use them to simplify our analysis. This is a significant assumption – the value of n changes non-trivially according to the boundary conditions chosen, and the peak stress goes as the square of n. However, one is hard pressed to find a value of n for non-classical boundary conditions, and as such, this is a necessary approximation.

Because the periodic boundary condition guarantees buckling in the second mode, we can begin to analyze these structures with the general form of Euler's criterion, given previously in Eq. 6. For the second mode $n = 2$, and thus the critical load is four times that of the first mode [17]. Divided by the total area of the RVE, we obtain the result for the peak stress,

$$\sigma_p = \frac{4\pi^2 EI}{A_{RVE} L^2} \tag{10}$$

The yield strength of FullCure 720 at a strain rate of 0.01, averaged across three samples, was experimentally determined to be 75.2 MPa [18]. This geometry buckles prior to that point.

The derivation of a spring constant from the geometry is difficult, since though we can calculate the lateral stiffness of the branches, they are not rigidly bound and therefore act as an elastic restraint on an elastic base for which we have no prediction. However, we can use the Timoshenko energy method for buckling to approximate an overall spring constant needed for each case to close the value gap, since the locations of the springs are already known for each multiple layer configuration.

The Timoshenko energy method uses a balance of energy at the limits of elastic stability to approximate a critical buckling load for a given structure [19]. This balance relies on the internal energy contained in a column that is compressed and bent (U) and the work done to the system (W). At the critical buckling load, these two quantities must be equal. The second mode deflection curve for a critical compressive load is

$$y = \delta \sin\left(\frac{2\pi x}{L}\right) \tag{12}$$

where δ is the amplitude of the deflection curve, or maximum deflection.
With this deflection, the bending strain energy of the column is

$$U = \frac{1}{2} EI \int_0^L \left(\frac{d^2 y}{dx^2}\right)^2 dx = \frac{4\delta^2 \pi^4}{L^3} EI \tag{13}$$

The displacement of the axial load point is

$$q = \frac{1}{2} \int_0^L \left(\frac{dy}{dx}\right)^2 dx = \frac{\delta^2 \pi^2}{L} \tag{14}$$

and therefore, since energy is equal to a force multiplied by the distance over which it acts,

$$W = Pq = \frac{\delta^2 \pi^2 P}{L} \tag{15}$$

The springs also store internal energy, and a stiffness k, and in this case, two springs at the maximum deflection points of the curve, yielding an energy expression

$$K = \frac{1}{2}k\delta^2 + \frac{1}{2}k\delta^2 = k\delta^2 \tag{16}$$

However, the springs resist the applied load, and therefore work in conjunction with the bending strain energy. Combining Eqs. 13, 14, and 16 yields the energy balance

$$U + K = W \tag{17}$$

$$\frac{4\delta^2\pi^4 EI}{L^3} + k\delta^2 = \frac{\delta^2\pi^2 P}{L} \tag{18}$$

Solving Eq. 16 for the load P and dividing by the RVE area, our modified critical buckling stress now has a reliance on a spring constant

$$\sigma_p = \frac{4\pi^2 EI}{A_{RVE}L^2} + \frac{kL}{A_{RVE}\pi^2} \tag{19}$$

However, this analytical model idealizes the bending modes of the structure, assuming that the modes do follow the deflection function in the shape of a full sine wave, which is not necessarily the case. The composites here can buckle in unanticipated wavelengths due to the unique boundary conditions, and a model that can account for the complexities of those deformations must be derived for each individual geometry. This analytical approach then serves to verify the trends in the simulations, and not to predict exact values. However, we can gather a full picture of the response of these structures using finite-element methods.

Chapter Three: Finite Element Based Micromechanical Modeling

3.1. Model Description

The structures were simulated and deformed using the finite element program ABAQUS/Standard. Twenty-four variations on the RVE were created to parametrically determine the effect of three variables: the volume fraction, coating fraction, and layer number.

The volume fractions approximate 5%, 10%, and 20% of the total RVE volume, corresponding to true volume fractions of 5.54%, 11.81%, and 19.83%. The exact volume fractions were determined from truss dimensions that would be simple to scale and fabricate via 3D printing. When the volume fraction is varied, only the cross-sectional area of the struts and branches change; the strut length l (see Figure 1) remains fixed at 7 mm for all simulations. The coating fraction t_c represents the percent of truss width taken up by the coating on each side. The coating fractions are 5%, 10%, and 20%. Therefore, t_c = 5% for a strut width of s=1 mm represents a coating of 50 um on each side – viewing a planar slice along the x-z plane, the total width of the coating is 100 um, and the width of the core is 900 um. Thus a change in the coating fraction does not change the overall volume fraction of the RVE; the total volume occupied by material is held constant. The layer number N is the number of repeat layers of the RVE. The models in this study contain from two to five layers, corresponding to RVE lengths L=14 mm, 21 mm, 28 mm, and 35 mm. When the layer number is varied, the area of the RVE does not change and is always fixed at 7 mm x 7 mm = 49 mm^2. The range of each parameter was chosen to allow for enough data to establish trends, but not so much as to render the establishment exhaustive.

The structural pattern of the material is a formation of cubic trusses. To obtain the macroscale deformation, it was necessary to deconstruct the overall structure into a series of repeated units, and then simulate the response of the unit instead of the whole. After the unit response is obtained, it is scaled back to the macroscale. And because the response of the unit cell, or representative volume element (RVE), is representative of the whole, this micromechanical modeling technique is aptly suited for a systematic study of varying parameters.

The RVE geometry is a large column with a square cross-section as shown in Figure 1. The column is oriented vertically with four "branch" protrusions of identical geometry oriented perpendicularly to the column, spaced evenly at 90 degrees about the column axis. Each group of four branches represents a layer. The two-layer RVE contains two groups of four branches. To obtain the coating elements, the original uncoated geometry was partitioned by a series of datum planes spaced inside of the truss surfaces at a distance equal to the coating fraction. The design schematic and meshed structure for a two layer RVE can be viewed in Figure 4. The entire structure was then defined as one material, and the partitioned coating sections were defined as a separate material. The material definitions are editable in the input files. The geometry was modeled with C3D8H hybrid elements. The number of nodes and elements in each model is dependent on the number of layers, and independent of the variations in volume fraction and coating fraction, since the element size was scaled to adapt to the larger RVEs. The simulation listing, with the number of nodes and elements in each model, appears below in Table 1.

Table 1: A listing of simulations run for the systematic study of varying volume fraction, coating fraction, and layer number.

Truss Width (mm)	Coating Thickness (um)	Volume Fraction	Coating Fraction	Layer Count	Nodes	Elements
1	0	5.54%	0%	2	6876	4750
1	0	5.54%	0%	3	10296	7125
1	0	5.54%	0%	4	13716	9500
1	0	5.54%	0%	5	17136	11875
1	50	5.54%	5%	2	12480	9506
1	50	5.54%	5%	3	18688	14259
1	50	5.54%	5%	4	24896	19012
1	50	5.54%	5%	5	31104	23765
1	100	5.54%	10%	2	12480	9506
1	100	5.54%	10%	3	18688	14259
1	100	5.54%	10%	4	24896	19012
1	100	5.54%	10%	5	31104	23765
1	200	5.54%	20%	2	12480	9506
1	200	5.54%	20%	3	18688	14259
1	200	5.54%	20%	4	24896	19012
1	200	5.54%	20%	5	31104	23765
1.5	0	11.81%	0%	2	6876	4750
1.5	75	11.81%	5%	2	12480	9506
1.5	150	11.81%	10%	2	12480	9506
1.5	300	11.81%	20%	2	12480	9506
2	0	19.83%	0%	2	6876	4750
2	100	19.83%	5%	2	12480	9506
2	200	19.83%	10%	2	12480	9506
2	400	19.83%	20%	2	12480	9506

Because the RVE must be a truly repeatable unit, the finite-element geometries were subject to specialized constraints. Periodic boundary conditions ensure that, for a structure subjected to any deformation, the RVE remains a repeatable element. For a block cell, the motion of opposing planes is limited to ensure that each pair could match if superimposed one to another. In the case of our RVE, the faces of the opposing truss branches are constrained to each other, as well as the opposing faces of the columns. This effect is demonstrated on a simple cube in Figure 6.

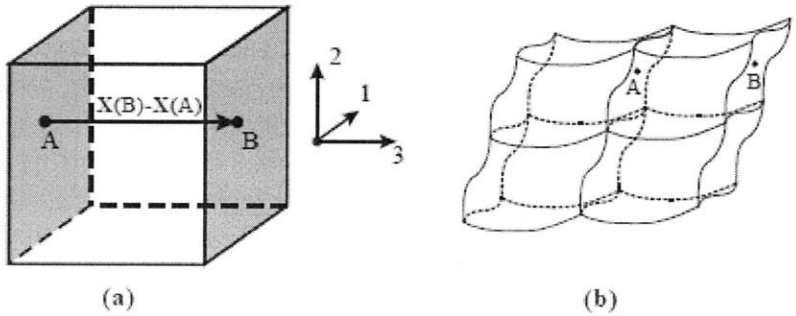

Figure 6: (a) Undeformed cubic structure with periodic boundary condition. (b) Deformed array of structures. Reprinted from "Periodic Boundary Condition for Representative Volume Elements" with permission of Dr. Lifeng Wang.

The conditions are represented by the following equation [20]:

$$\mathbf{u}(B) - \mathbf{u}(A) = (\mathbf{F} - \mathbf{1})\{\mathbf{X}(B) - \mathbf{X}(A)\} \tag{20}$$

where $\mathbf{u}(A)$ and $\mathbf{u}(B)$ are the displacement vectors for each face, $\mathbf{F}$ is the macroscopic deformation gradient, 1 is the second order identity tensor, and $\mathbf{X}(A)$ and $\mathbf{X}(B)$are the reference coordinates of each point. In this case, $(\mathbf{F} - \mathbf{1})$ is equal to the macroscopic strain ϵ. This equation effectively constrains each face to a displacement that is based solely upon the macroscopic displacement of the total RVE, and in turn, constrains the faces to the same angle (as discussed in 2.2.2). An algorithm was developed in MATLAB for the automatic assignment of periodic boundary conditions to square cells [21-23]. The algorithm developed here executes a series of consecutive loops that determines the node extrema in each axis, which comprise the external faces of the RVE, and removes any double- or triple-counted nodes on edges and corners. The selected nodes are then sorted by the magnitude of each coordinate value, and then input into groups comprising each of the six faces, twelve edges, and eight corners of the cubic cell. Periodic boundary conditions are applied to opposing node groups in the form of a displacement equation, constraining the opposing nodes to their original displacement in the undeformed RVE. For the RVEs considered here, the displacement in the x- and z-axis is 7 mm, and the y-axis between 14 mm (for a two-layer RVE) and 35 mm (for a five-layer RVE).

To accurately determine the initial modulus and the peak stress in the RVE, a compressive load was applied to the nodes comprising the top plane. Initially simulations were run to an engineering strain of 0.30; however, since all of the composite RVEs reach a peak stress well within a strain of 0.10, certain simulations that had difficulties with convergence were run to that strain level.

The general use finite-element software ABAQUS/CAE allows for a comprehensive buckling simulations with high-detail material definitions. The general procedure used here to establish a simulation is outlined below.

1. Define and mesh RVE geometry
2. Run RVE nodes through periodic boundary condition algorithm and recombine results to input file
3. Define an eigenvalue analysis to determine structural mode shapes
4. Define a postbuckling analysis to apply a compressive deformation in the selected mode shapes
5. Obtain nodal force & strain results from the output file

The definition of the geometry and mesh through the use of the periodic boundary condition algorithm has been covered in a previous section; this section elaborates on the remainder of the analysis.

ABAQUS/CAE automatically generates an input file given a few trivial adjustments to the Model Database, but the functional file was obtained through manual edits. After defining two steps (an initial step and general static analysis step), and field output and history output requests (stresses, strains, displacements and forces), a base input file was written. The node relations from the periodic boundary condition algorithm were added to the file, as well as general node sets defining the spatial planes of the rectangular cell. The general static analysis step was converted to a buckling analysis step considering the first 10 eigenvalues, using 20 eigenvectors in the iteration, and possessing a very high iteration limit. The output of this file was the first 10 mode shapes for the buckling analysis, the first of which was then fed into a separate input file.

To conduct the buckling analysis, first a mode was selected from the eigenvalue analysis, and then a small imperfection inserted into the RVE geometry based on the chosen mode shape. The size of the imperfection for all simulations was 20 um. A compressive load was then applied along the axis of the column through a strain-imposing boundary condition, which applied a total engineering strain of either 0.10 or 0.30 to the top plane across 10 or 30 steps, with each step equal to a second in time. The strain rate for all simulations was therefore 0.01 s^{-1}. A node in the simulation was fixed in all translational degrees of freedom so that the RVE could not translate in free space.

After the simulation was complete, the nodal force on the top plane and the total strain of the RVE were gathered from the history output, the force was divided by the volume of the RVE, and both quantities were plotted as an engineering stress-strain curve.

3.2. Results

A parametric approach was taken to examine the effect the three variables of interest: volume fraction V_f, coating fraction t_c and number of layers N. First, to analyze the effect of volume fraction and number of layers on a control structure, images of the deformed structure and simulation results for single-material geometries for FullCure 720 and Tango Plus are presented. Following that, the composite images and results are presented and the effect of the coating fraction t_c is analyzed.

3.2.1. FullCure 720

The FullCure 720 structures were simulated as an upper bound for the composites. Figure 7 displays images of the deformed polymer structures for each case simulated. In Figure 7a, the two-layer RVE deforms almost perfectly, matching the sine-wave displacement function. In Figure 7b, it is apparent that the deformation deviates from the ideal displacement function; the first full strut follows the sine-wave, but the last strut remains only slightly bent. In Figure 7c, only the middle strut buckles according to the sine-wave, with both the top and bottom struts relatively unaffected. In Figure 7d, all of the full struts are relatively straight and undeformed; they form a distinct angle with the support struts, and the half-struts at the top and bottom of the RVE deform instead. In Figure 7e, one can find a similar method of deformation as in Figure 7a; and in Figure 7f, the same is true, though the much wider strut width results in a less developed buckling deformation at comparable strains.

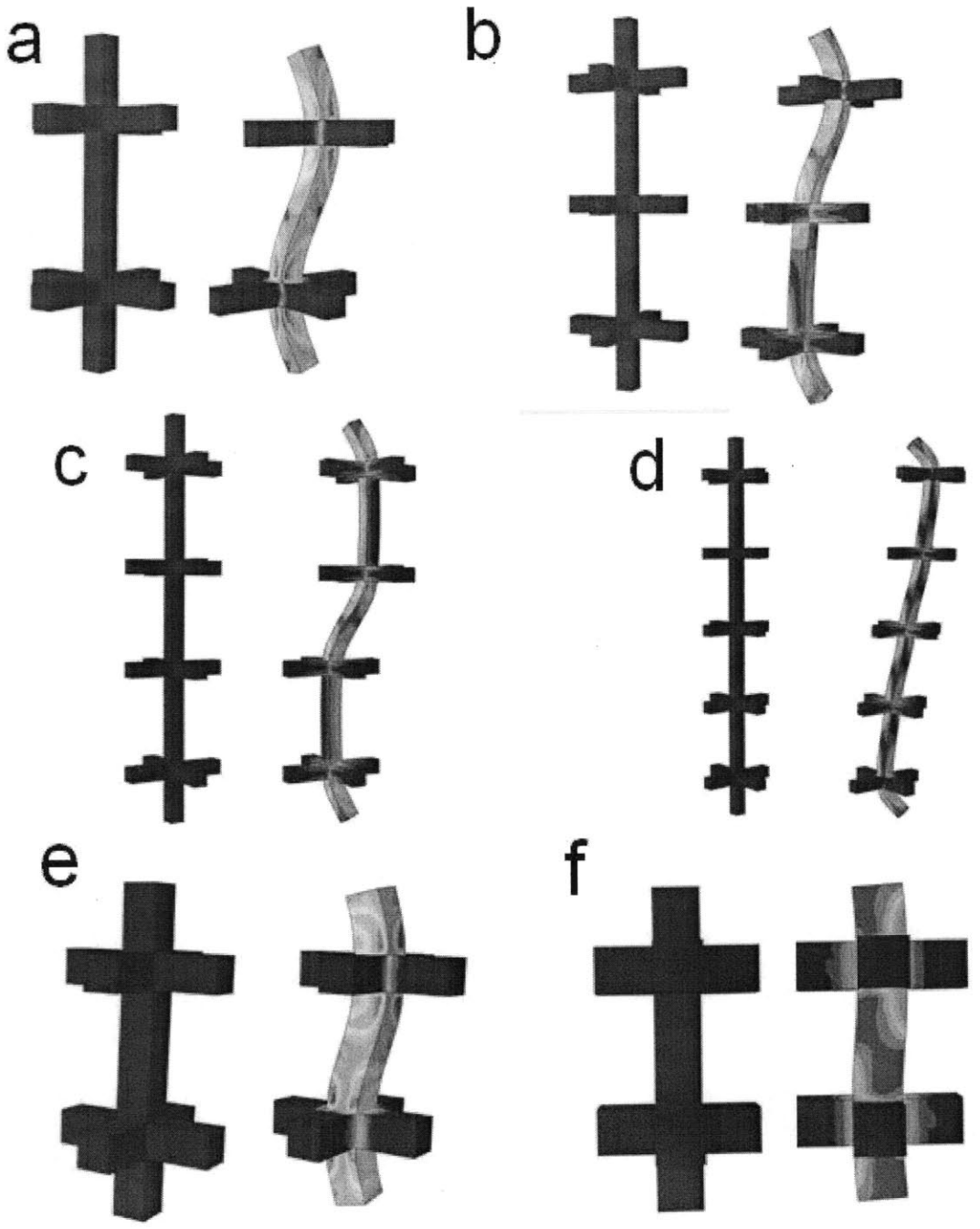

Figure 7: Deformed FullCure 720 structures at 5% strain with Mises' stress in contour. (a) $V_f = 0.05$, $N = 2$. (b) $V_f = 0.05$, $N = 3$. (c) $V_f = 0.05$, $N = 4$. (d) $V_f = 0.05$, $N = 5$. (e) $V_f = 0.10$, $N = 2$. (f) $V_f = 0.20$, $N = 2$.

The stress-strain curves for the FullCure 720 samples appear below. Figure 8 displays the results with the layer number N held constant and volume fraction varied from 0.05 to 0.10 to 0.20. The polymer buckles at higher strains with increasing volume fraction, and the buckling peak becomes more pronounced as the strut width increases.

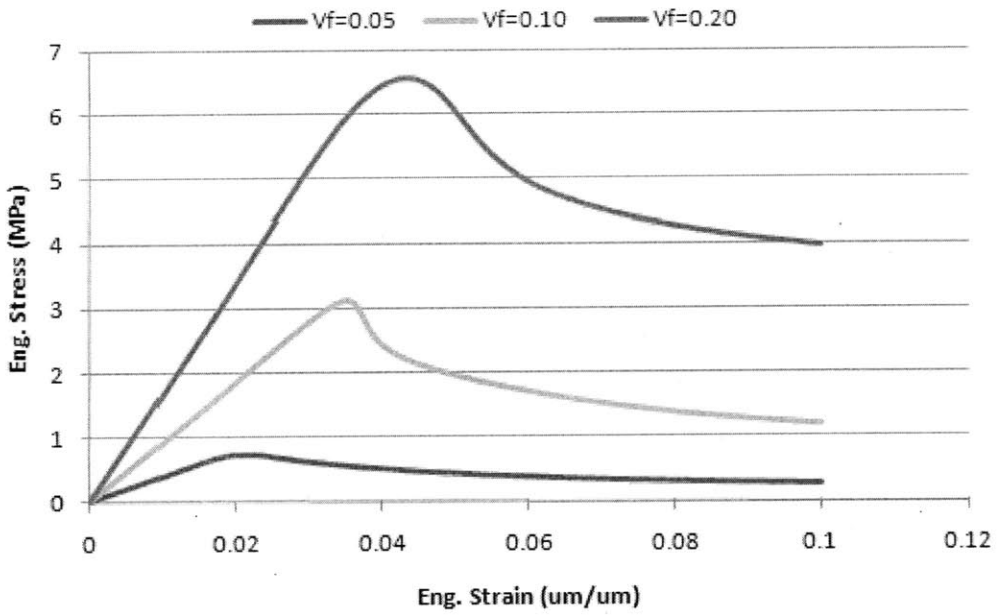

Figure 8: Stress-strain curves plotted for FullCure 720 simulations with $N = 2$ and varying volume fractions.

Figure 9 displays the results with the volume fraction held constant and layer number varied from N=2 to N=5. The modulus is identical for each sample; the buckling event occurs at lower strain with increasing layer number. The unique peak of the N=5 simulation corresponds to the non-ideal buckling of the half struts.

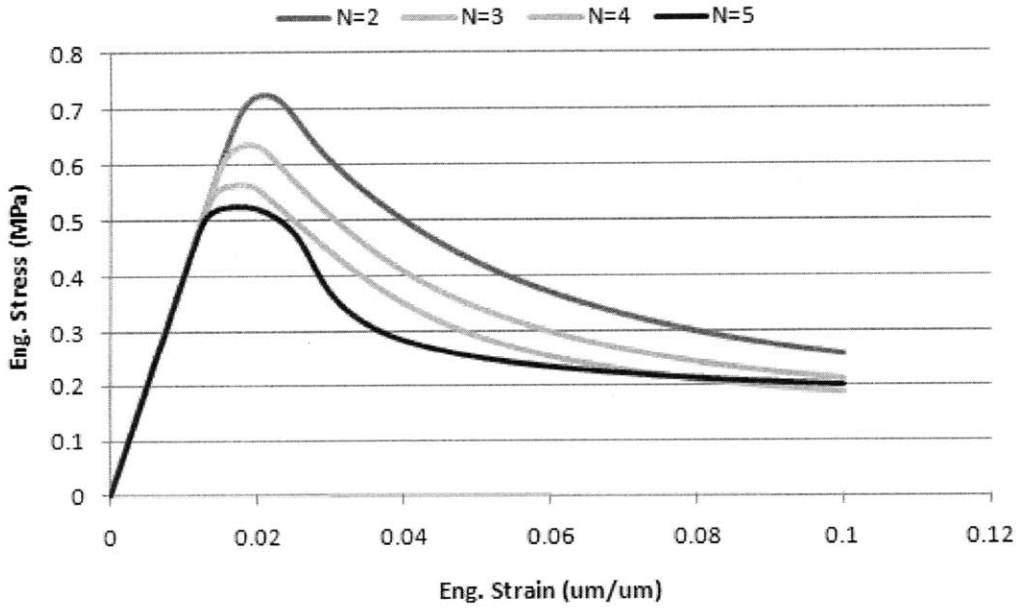

Figure 9: Stress-strain curves plotted for FullCure 720 simulations with $V_f = 0.05$ and varying layer numbers.

Figure 10 plots the modulus of the RVE against the volume fraction. The stiffness scales linearly with the volume fraction, since both the modulus and volume fraction scale with the square of the side length.

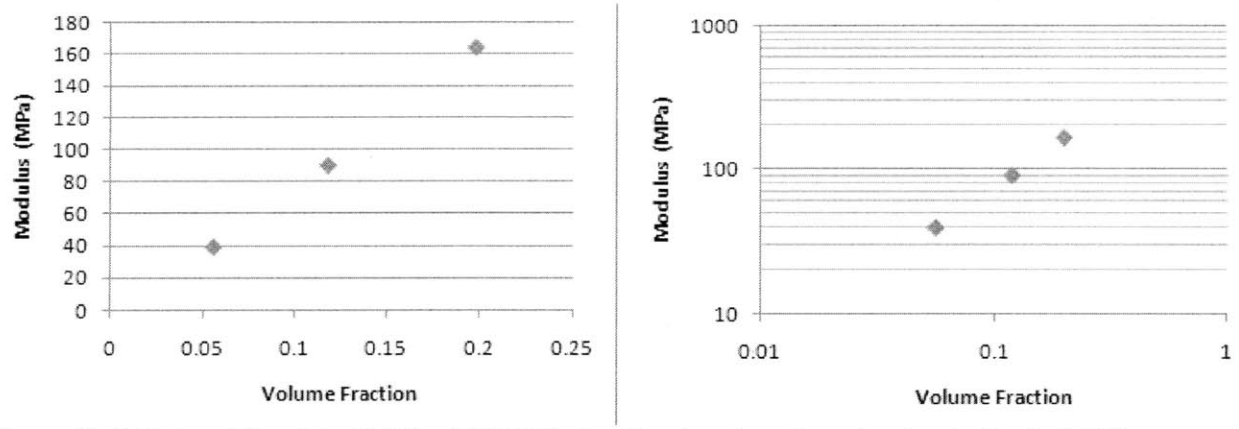

Figure 10: Initial modulus of the FullCure 720 RVE plotted against the volume fraction for $N = 2$. *left* Linear axes. *right* Logarithmic axes.

Figure 11 plots the peak stress against the volume fraction. The peak stress scales non-linearly with the volume fraction, since the modulus scales linearly with the volume fraction, but the second moment of area scales with the fourth power of the side length and the peak stress has an inverse square dependence on the effective buckling length. Though it is clear from viewing the deformation images in Figure 6 that not all of the simulations deformed in the ideal buckling mode, the peak stress that the structures must reach to deform is a limit, and must be reached either locally or globally before a structure can deform, regardless of non-uniformities in the mode.

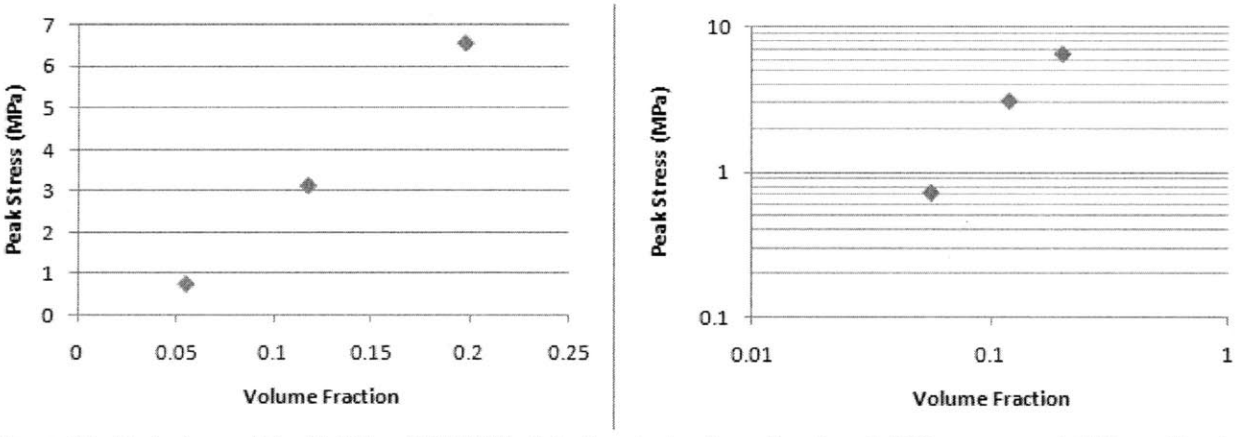

Figure 11: Peak stress of the FullCure 720 RVE plotted against volume fraction. *left* Linear axes. *right* Logarithmic axes.

Figure 12 plots the peak stress against the layer number. The peak stress decreases non-linearly with increasing layer number, corresponding to the inverse square dependence on the effective buckling length of the column. Ideally, one would expect a much more defined quadratic curve; however, the deformed images in Figure 6 clearly display buckling that does not follow the ideal sine-wave displacement function. The effective buckling length in this case is then reduced, and as such the decrease across layer number is less pronounced. The results for N=2 through N=5 demonstrate an approach to an asymptotic value as N increases; eventually the buckling strength will settle at a "floor" value at some high N.

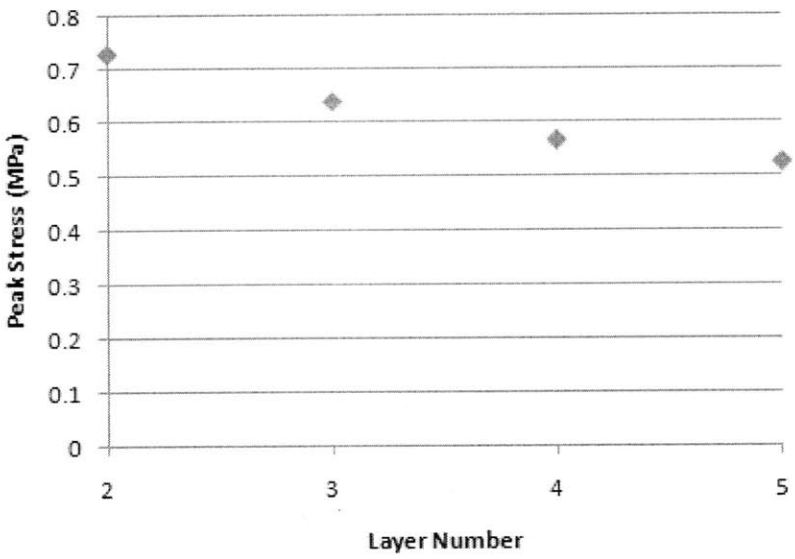

Figure 12: Peak stress of the FullCure 720 RVE plotted against layer number for $V_f = 0.05$.

3.2.2. Tango Plus

The Tango Plus structures were simulated as a lower bound to the composite structures. Figure 13 displays images of the deformed elastomer RVEs for each case simulated. Figure 13a shows the near-ideal deformation of the two-layer RVE. In Figure 13b, the top strut of the three-layer RVE buckles ideally but the bottom strut simply bends. Figure 13c showcases the deformation of the four-layer RVE, where some degree of buckling is apparent in every strut. In Figure 13d, every strut except for the top strut buckles. Figures 13e and 13f show the larger two volume fractions for a two-layer RVE, which mirror the deformation of Figure 13a.

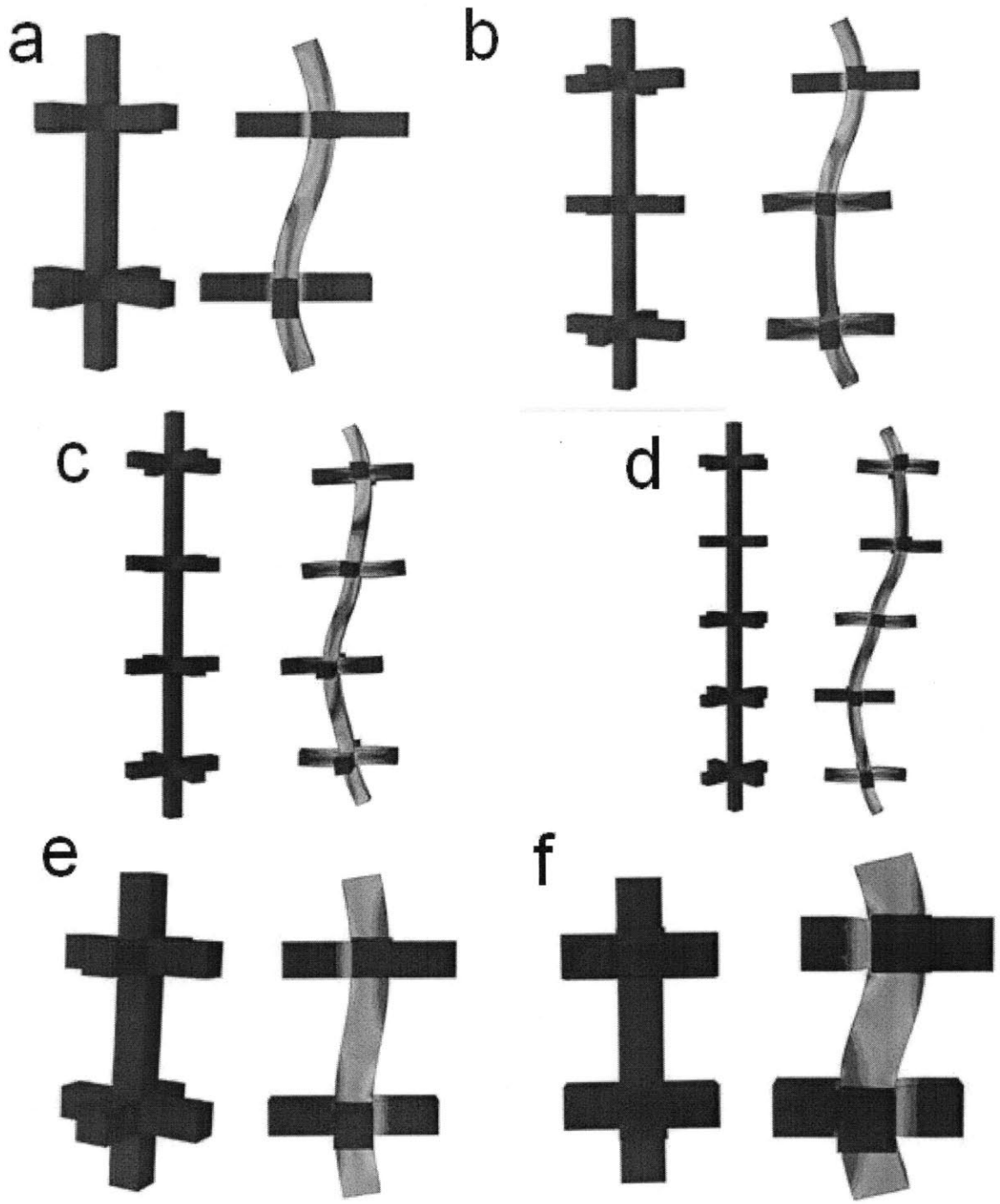

Figure 13: Deformed Tango Plus structures at 5% strain with Mises' stress in contour. (a) $V_f = 0.05$, $N = 2$. (b) $V_f = 0.05$, $N = 3$. (c) $V_f = 0.05$, $N = 4$. (d) $V_f = 0.05$, $N = 5$. (e) $V_f = 0.10$, $N = 2$. (f) $V_f = 0.20$, $N = 2$ (10% strain).

The stress-strain curves for the Tango Plus samples appear below. Figure 14 displays the results with layer number held constant and volume fraction varied. Like with the FullCure 720 samples, the buckling event occurs at a later strain with the increase of the volume fraction.

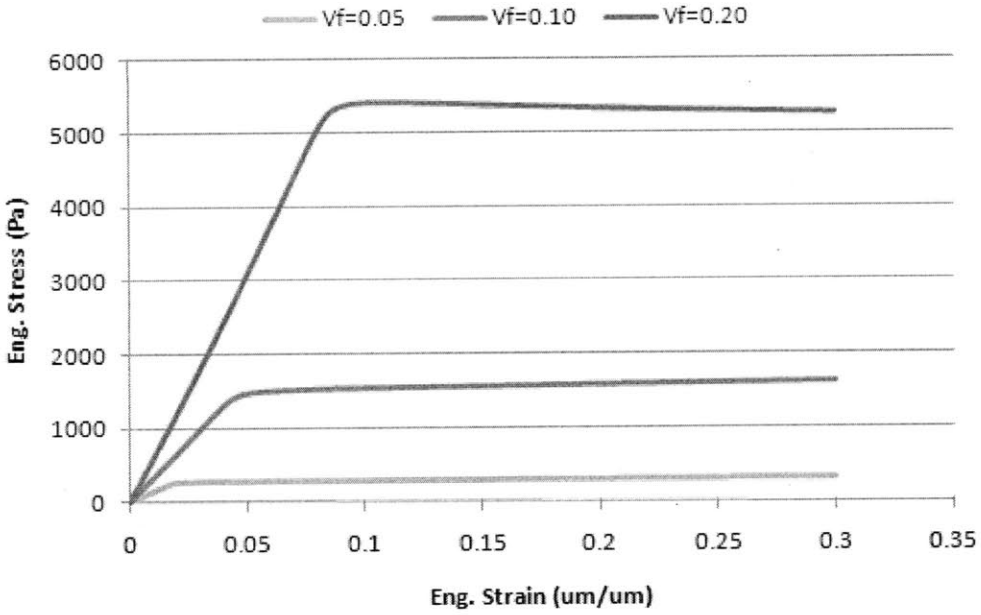

Figure 14: Stress-strain curves plotted for Tango Plus simulations with $N = 2$ and varying volume fractions.

Figure 15 displays the results with the volume fraction held constant and layer number varied. The peak stress occurs at a slightly smaller strain with increasing layer number, corresponding to a lower peak stress along the shared elastic modulus, which is in turn caused by an increase in the effective buckling length. The intersection of the stress-strain curves at higher strains is likely caused by the non-buckling strut in the five-layer RVE.

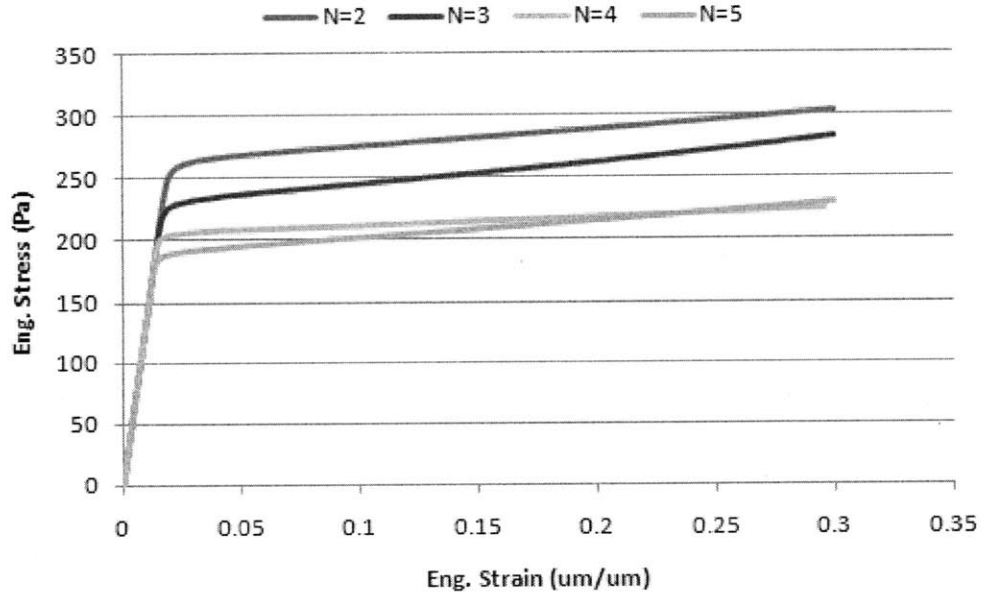

Figure 15: Stress-strain curves plotted for Tango Plus simulations with $V_f = 0.05$ and varying layer numbers.

Figure 16 plots the modulus of the RVE against the volume fraction. The modulus scales with the area of the strut. The dependence is linear as both the volume fraction and modulus depend on the square of the strut width.

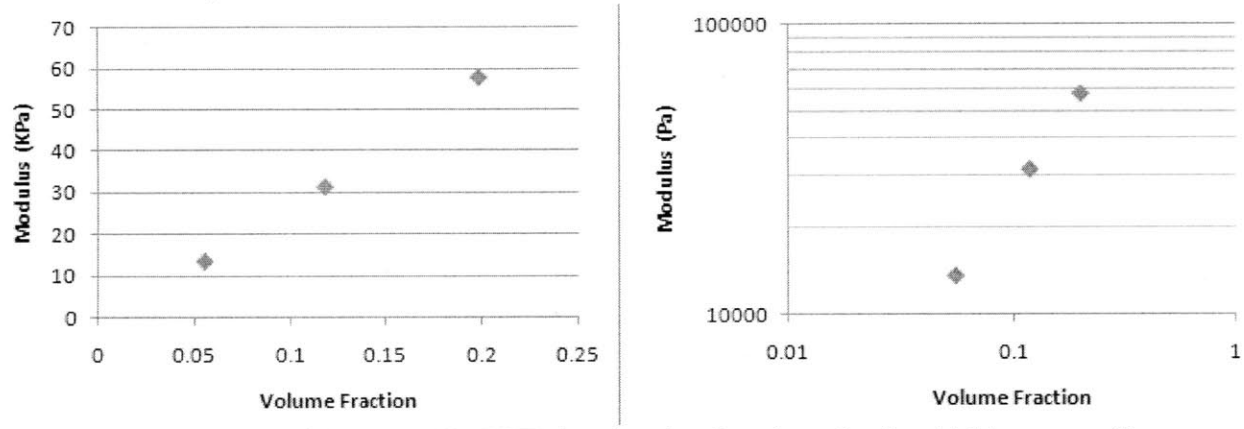

Figure 16: Initial modulus of the Tango Plus RVE plotted against the volume fraction. (a) Linear axes. (b) Logarithmic axes.

Figure 17 plots the peak stress against the volume fraction. As was discussed in 3.2.1., the peak stress varies non-linearly with the volume fraction. A nonlinear dependence is clear from the plots, and the deformation images in Figures 13a, 13e, and 13f deform in the same manner.

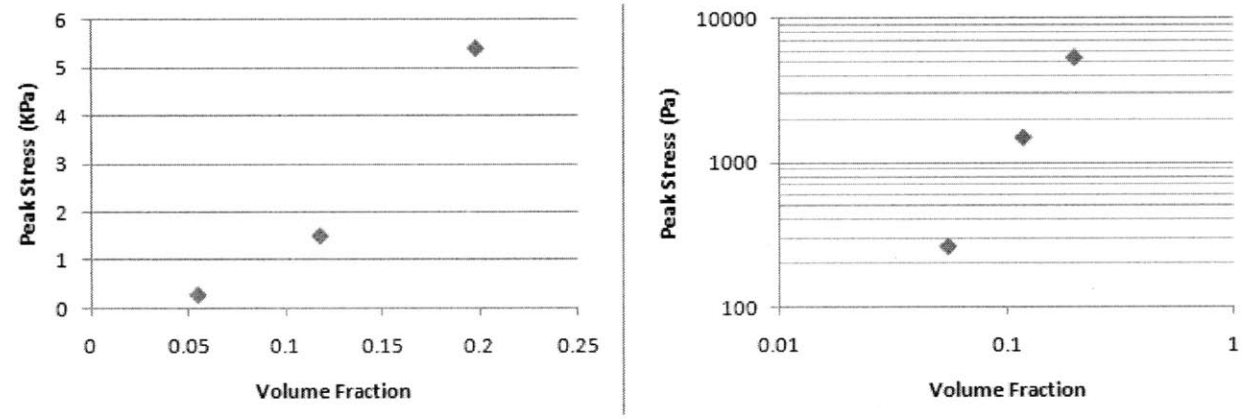

Figure 17: Peak stress of the Tango Plus RVE plotted against volume fraction. (a) Linear axes. (b) Logarithmic axes.

Figure 18 plots the peak stress against the layer number. The dependence is quadratic upon the effective buckling length of the structure, but again not as pronounced as one would expect due to the influence of the support branches and the reduction of the effective buckling length with increasing layer number.

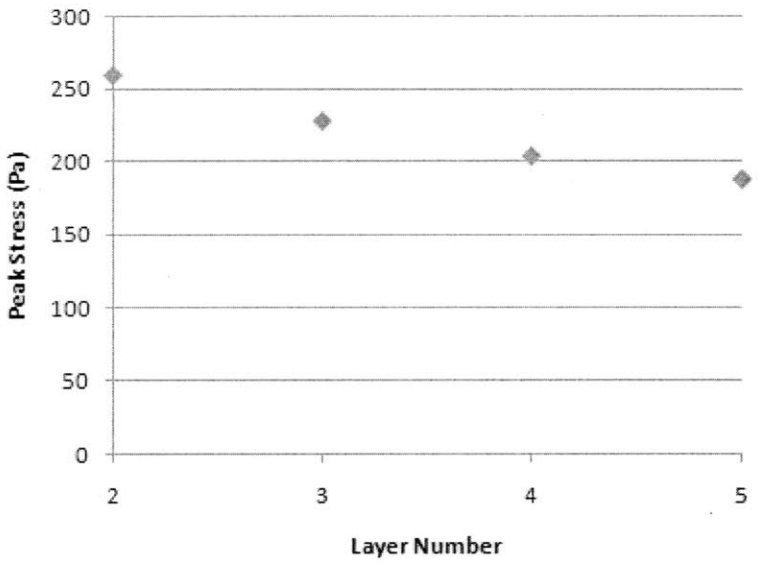

Figure 18: Peak stress of the Tango Plus RVE plotted against layer number.

3.2.3. Composites

With the upper and lower bounds defined, the composite structures were simulated in a similar manner. Figure 19 displays images of the deformed composite RVEs for each case simulated. Figure 19a displays the buckling mode of the two-layer RVE for a $V_f = 0.05$ and $t_c = 0.05$. It is clear that yielding of the polymer coating causes a non-ideal deformation after the buckling event. In Figure 19b, the top strut bends while the bottom strut buckles. In both Figures 19c and 19d, the struts appear relatively rigid save for some small bending; the buckling and subsequent yielding occurs at the stress concentrations at the strut-branch interfaces.

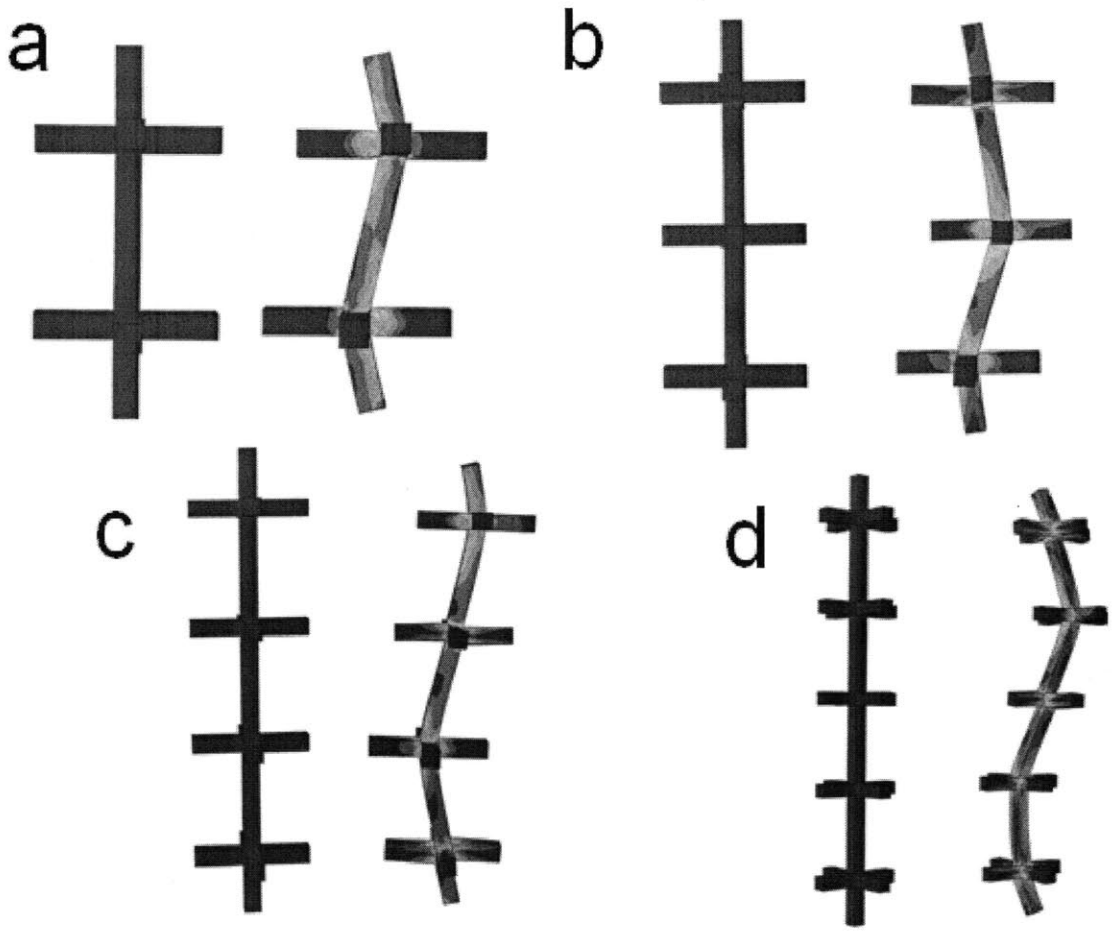

Figure 19: Deformed composite structures at 5% strain with Mises' stress in contour for volume fraction $V_f = 0.05$ and coating fraction $t_c = 0.05$. (a) $N = 2$. (b), $N = 3$. (c) $N = 4$. (d) $N = 5$.

The stress-strain curves for the composite samples appear below. Figure 20 displays the results with volume fraction held constant and coating fraction varied and layer number varied. The buckling peaks here as much "sharper" than in the FullCure 720 or Tango Plus simulations; this is caused by the subsequent yielding of the polymer at the strut-branch interface that reduces the stiffness of the sample over a short strain range; the plateau that the stress-strain curves approach is affected by the elastomeric core as well as the yielded polymer, which are now of comparable stiffness. The previous effects with increasing layer number are again seen with the composite samples.

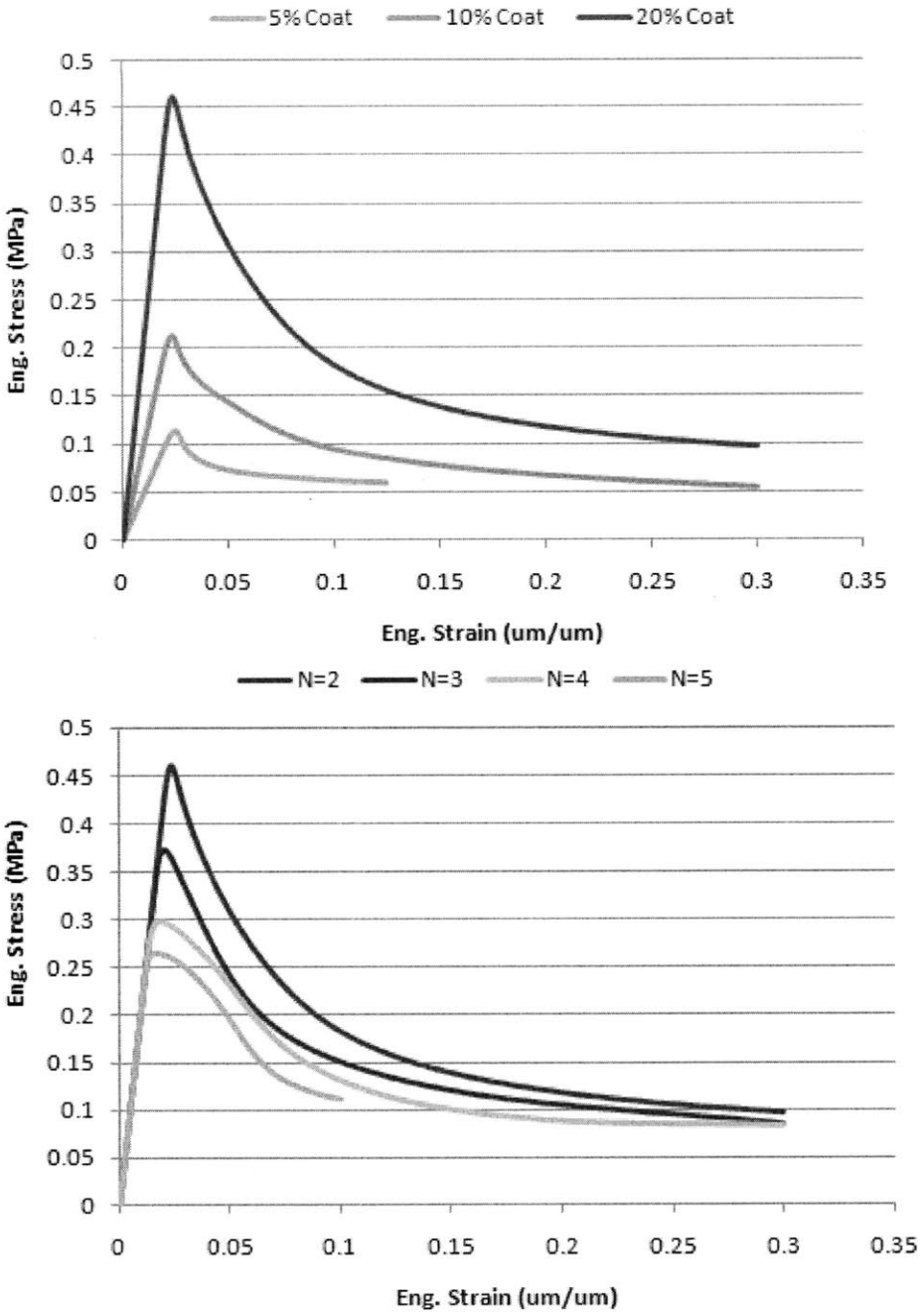

Figure 20: Stress-strain curves plotted for composite simulations with a volume fraction of 0.20 and *top* $N = 2$ with varying coating fractions; *bottom* $t_c = 5\%$ and varying layer numbers.

Figure 21 displays the results with the coating fraction held constant and volume fraction varied and layer number varied. The buckling peak occurs at a higher strain with the increase of the volume fraction, just as with the polymer and elastomer simulations. The trends expressed in those previous sections all hold for the composite simulations seen here.

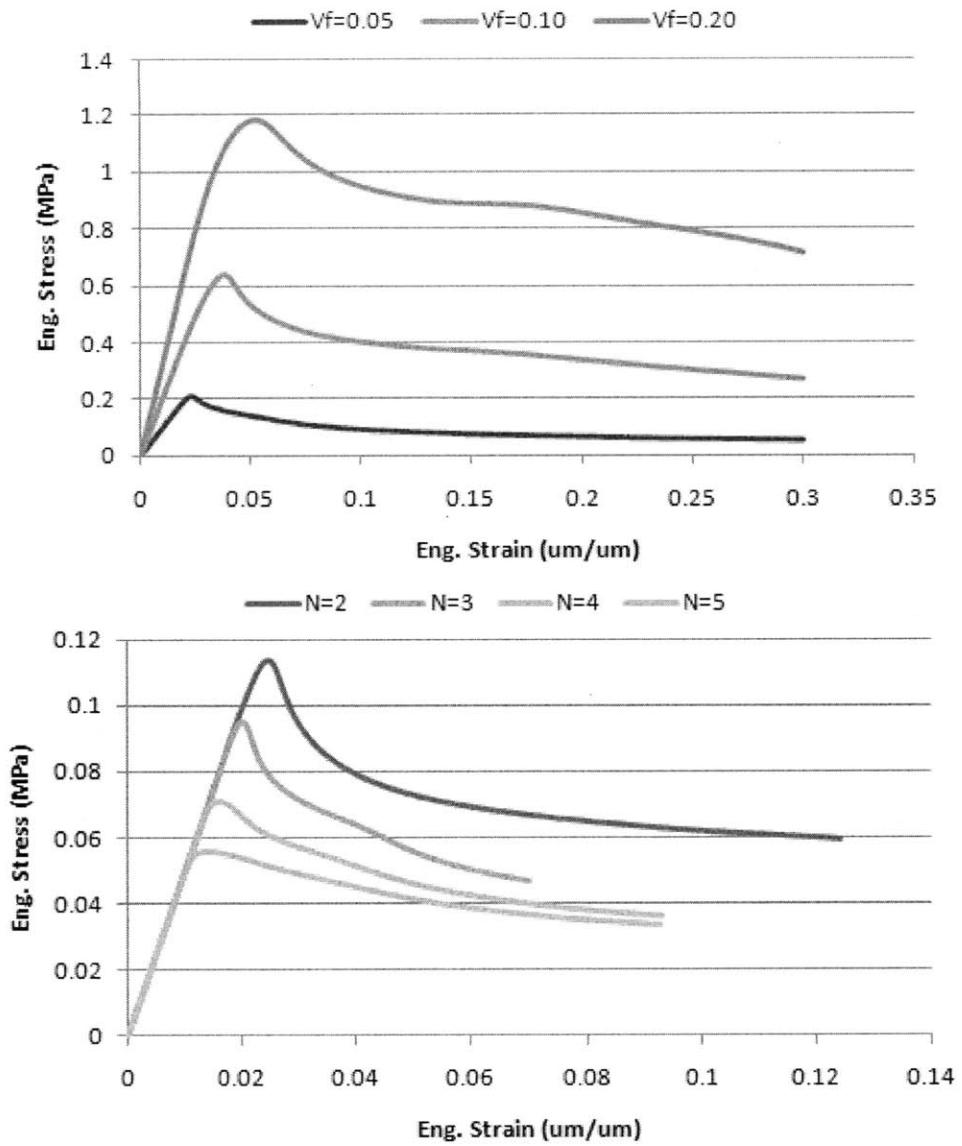

Figure 21: Stress-strain curves plotted for composite simulations with a coating fraction of 0.10 and *top* with $N = 2$ and varying volume fractions; *bottom* with $V_f = 0.05$ and varying layer numbers.

Figure 22 plots the modulus of the RVE against the coating fraction for each volume fraction, and vice versa. Increasing the coating fraction increases the coating thickness *t,* for which the modulus has a non-linear dependence (there is a quadratic term and a linear term, where the linear term dominates for high volume fractions). Increasing the volume fraction increases the square of the strut length, which increases the square of the coating thickness with the coating fraction held constant, resulting in a modulus dependence on t that scales to the second and fourth powers, or a dependence on V_f that is both linear and to the square, with the linear term again dominating for high volume fractions.

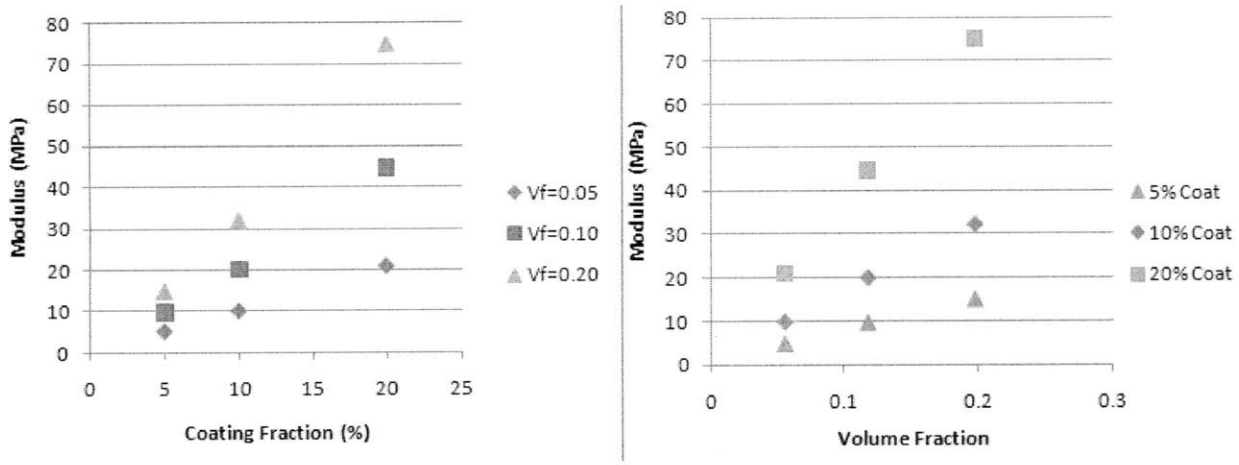

Figure 22: *left* Modulus values plotted against coating fraction for all volume fractions. *right* Modulus values against volume fraction for all coating fractions.

Figure 23 plots the peak stress against the volume fraction. An increase in the coating fraction causes an increase in the coating thickness t, and an increase in the volume fraction causes an increase in the strut width s, both of which scale non-linearly with the second moment of area with which the peak stress varies directly. Thus an increase in either the coating fraction with volume fraction held constant or volume fraction with coating fraction held constant serves to enlarge the polymer area, causing the peak stress to rise.

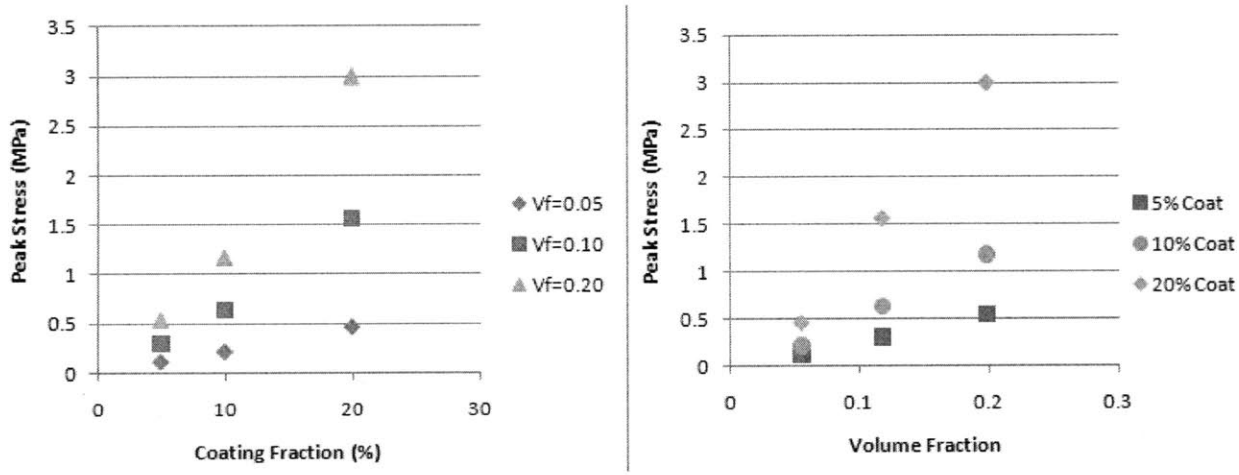

Figure 23: *left* Peak stress of the composite plotted against coating fraction for all volume fractions ($N = 2$). *right* Peak stress against volume fraction for all coating fractions ($N = 2$).

Figure 24 plots the peak stress against the layer number for each coating fraction. The same decreasing non-linear dependence that was seen for the FullCure 720 and Tango Plus samples is seen here. When viewed closely, the trend does not appear quite quadratic; this is due to the variations in the buckling deformations between the even-layered and odd-layered RVEs. With the composites, the branches appear to have a more pronounced effect on the buckling mode, and one can see in Figure 24 that the values for N=3 and N=5 are slightly raised from the decreasing non-linear curve (see Figures 11 and 16 for comparison).

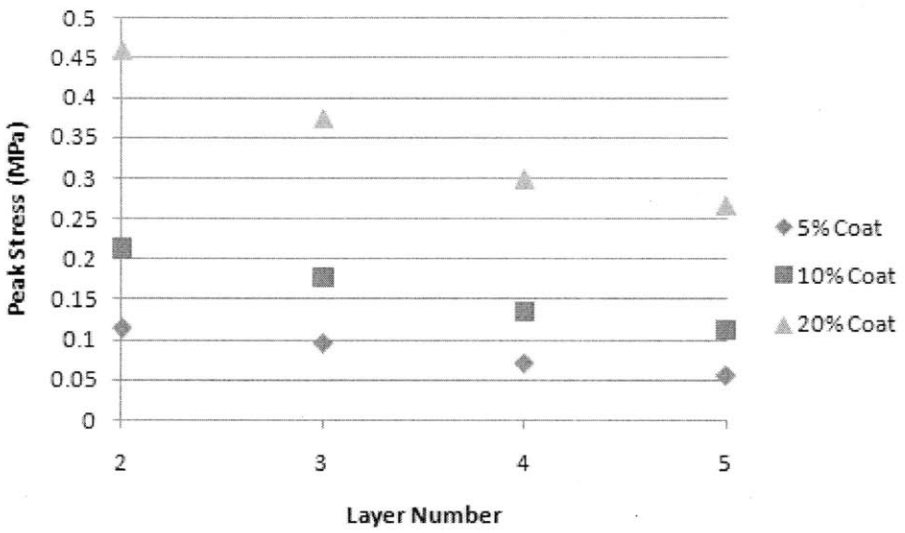

Figure 24: Peak stress plotted against layer number for a volume fraction of 0.05 and all coating fractions.

Figure 25 compares the analytical and simulated modulus values for $V_f = 0.05$, $N = 2$ and varying coating fractions. The slight deviation in the simulated values from the derived moduli could be accounted for by the imperfection required by the finite-element buckling procedures. A small lateral displacement is input at the critical points in the buckling mode – for this case, at the peak and valley of the sine wave. This means that the column is actually always in a state of bending, which lowers the modulus of the part.

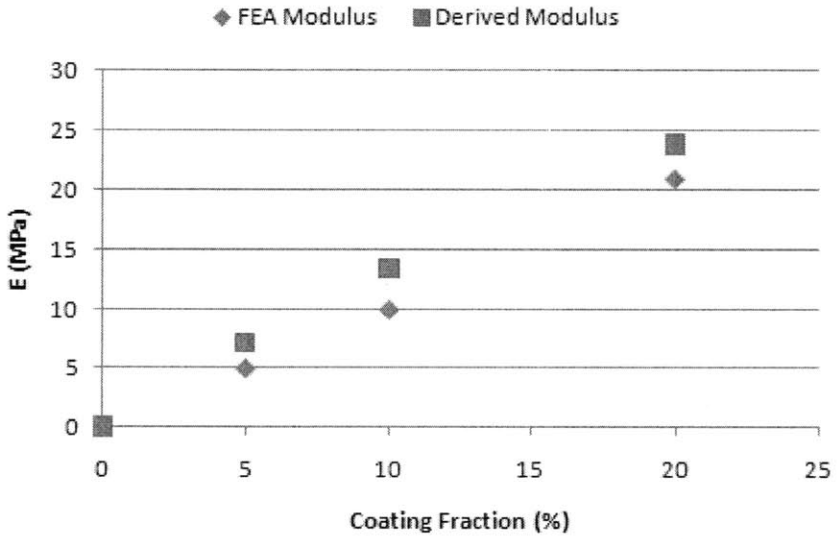

Figure 25: Analytical and simulated modulus values plotted against coating fraction for the volume fraction of 0.05.

Figure 26 compares the analytical and simulated results for peak stress for $V_f = 0.05$ and $t_c = 0.05$ with varying layer numbers. As can be seen in Figure 19, the simulations do not buckle in the classical mode and thus in order to have a decent amount of agreement between the results one must determine the effective length by analyzing the behavior of the different struts in the deformation images. There is significant bending in many of the figures beginning at the strut-

branch interfaces, which in the case of the composites serve as buckling points. The effective buckling length is modeled here as L = 19mm, 21mm, 23mm, and 25mm for N = 2, 3, 4, and 5, respectively. Results with these values appear in Figure 26.

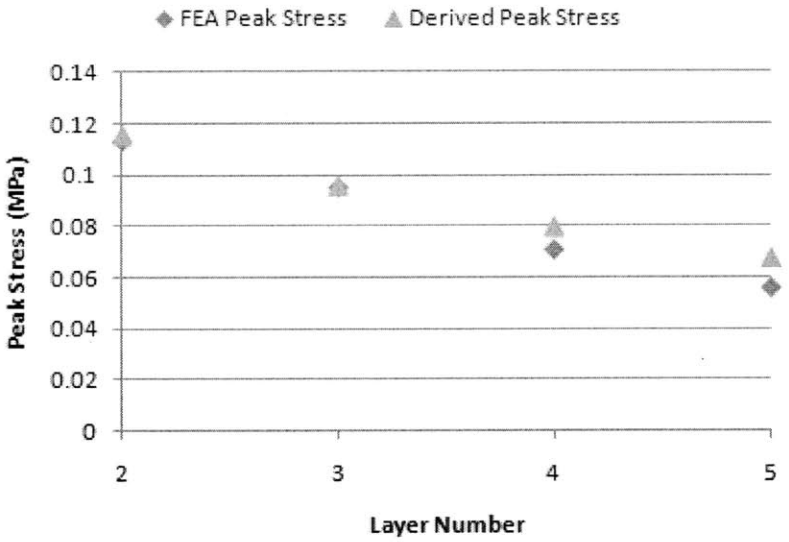

Figure 26: Analytical and simulated peak stress values plotted against layer number for a volume fraction of 0.05 and coating fraction of 0.05.

Chapter Four: Fabrication and Testing of Periodic Structures

4.1. Fabrication of Structures

For the verification of the finite-element models, select truss structures were fabricated and mechanically tested. Because the structures possess a geometry that is impossible to fabricate by conventional methods, cubic samples were designed in SolidWorks and 3D printed. Fabrication was conducted on the Objet Connex 500, a commercial 3D printer that can build a structure with dual materials simultaneously [24]. After printing is complete, the samples are completely encased in support material; it is necessary to remove this material by means of probing tools and a pressurized water jet.

The samples were designed from the linear patterning of four-layer RVEs to form a cubic structure. Base plates were designed to hold the structure together and provide a smooth surface for compression testing. The samples are not perfect cubes – the base plate skews the vertical dimension to render geometry of 28 mm x 28 mm x 30 mm.

Six groups of samples were fabricated – pure FullCure 720, pure Tango Plus, and composite versions for volume fractions of 0.10 and 0.20. The composite versions had a coating fraction of 20%. Only two variations on the composite sample were able to be printed given restrictions on the 3D printing fabrication process – the minimum coating thickness of the printer was 0.3 mm, and features could not be printed smaller than that dimension. Though all samples were printed and tested to verify the simulation, the pure samples were printed to bound the composite results, and also to provide an alternate method of verification since the geometry of the composite samples was on the edge of the printer resolution. The CAD geometry and samples appear in Figure 27.

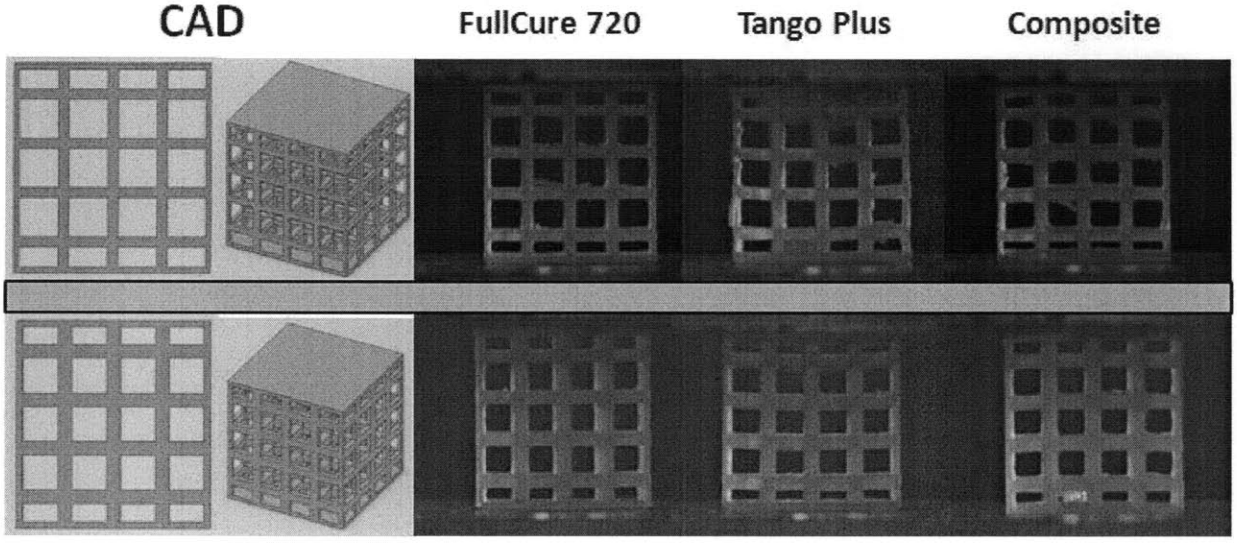

Figure 27: The 3D printed structures and the CAD geometry from whence they came.

4.2. Testing Protocol

Three identical samples were printed for each configuration, and tested consecutively. Each sample was tested in uniaxial compression on a Zwick mechanical tester with a 10 kN load

cell. The sample was subjected to uniaxial compression in a displacement-controlled condition whereby the compression platens are displaced at a strain rate of 0.01 for each sample. Because the samples all had approximately the same dimensions, the same standard travel of 20 mm was applied to each test, resulting in a maximum strain of about 0.67.

4.3. Results

The dimensions of each sample were at a slight variance from the design; in all cases, the side length of the samples was slightly oversized (from 0.1 to 0.5 mm), and the height was slightly undersized (from 0.4 mm to 1.3 mm). Measurements were taken with a digital caliper with a resolution of 0.01 mm.

4.3.1. FullCure720

The FullCure 720 samples demonstrated fairly repeatable results. The modulus of both volume fractions correlated well with the simulations; the peak stress did not match as well. For the 0.20 volume fraction, the simulated modulus was 165 MPa, against an experimental modulus of 170 MPa; for the 0.10 volume fraction, the simulated modulus was 90 MPa against 87.5 MPa in testing. The simulated peak stress for the 0.20 volume fraction was 6.55 MPa as compared to an experimental peak stress of 5.54 MPa. The 0.10 volume fraction simulation did not correspond so well; the simulated peak stress was 2.92 MPa as compared to an experimental peak stress of 2.02 MPa. Figures 28 and 29 display the simulated curves against the experimental response.

It is most likely that imperfections from the printing process as well as a loading condition that is not perfectly axial both contribute to disparity in peak stress. Imperfections could reduce the coated area significantly, upon which the peak stress strongly depends. In addition, given the porous geometry of the cellular solid and the thin strut width, the FullCure 720 samples did not just yield but completely fractured upon loading. When the struts bend, half of the strut bends in tension, which causes failure at an earlier stage than if they were purely compressed.

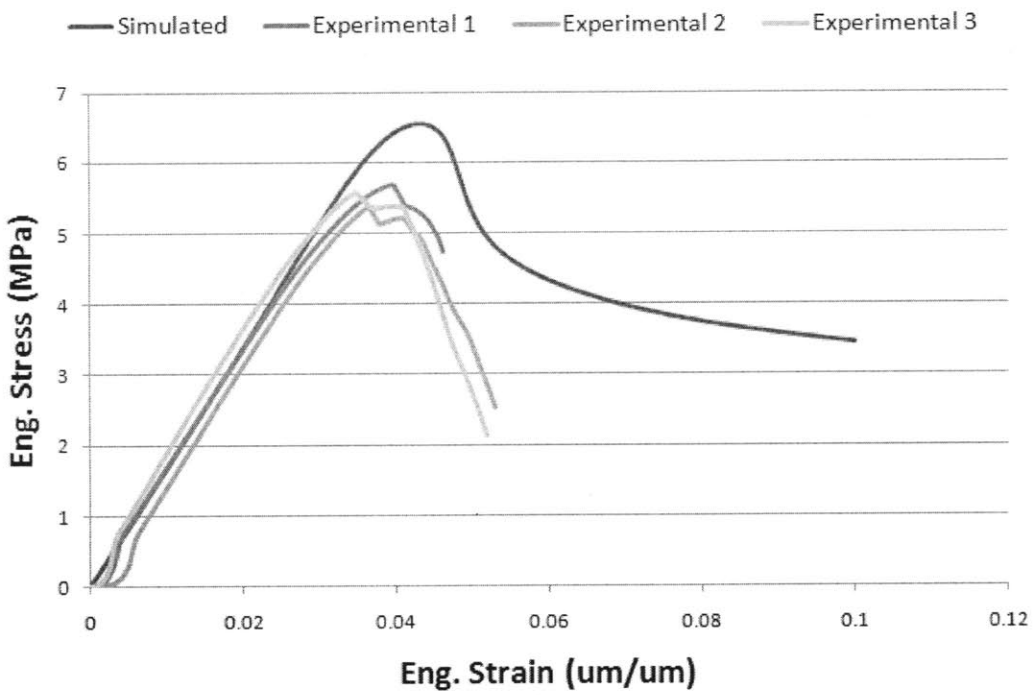

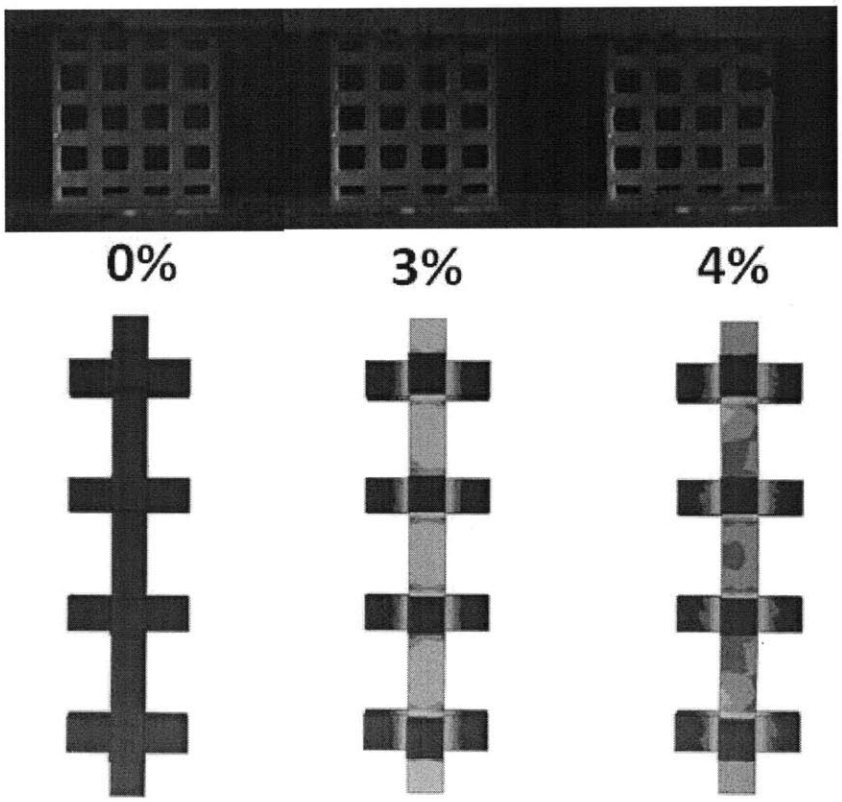

Figure 28: *top* Comparison of simulated and experimental results for a FullCure 720 four-layer structure with a volume fraction of 0.20. *bottom* Test photos and simulation geometry are compared for given strain levels at the initial stage, pre-buckling, post-buckling, and buckled conditions.

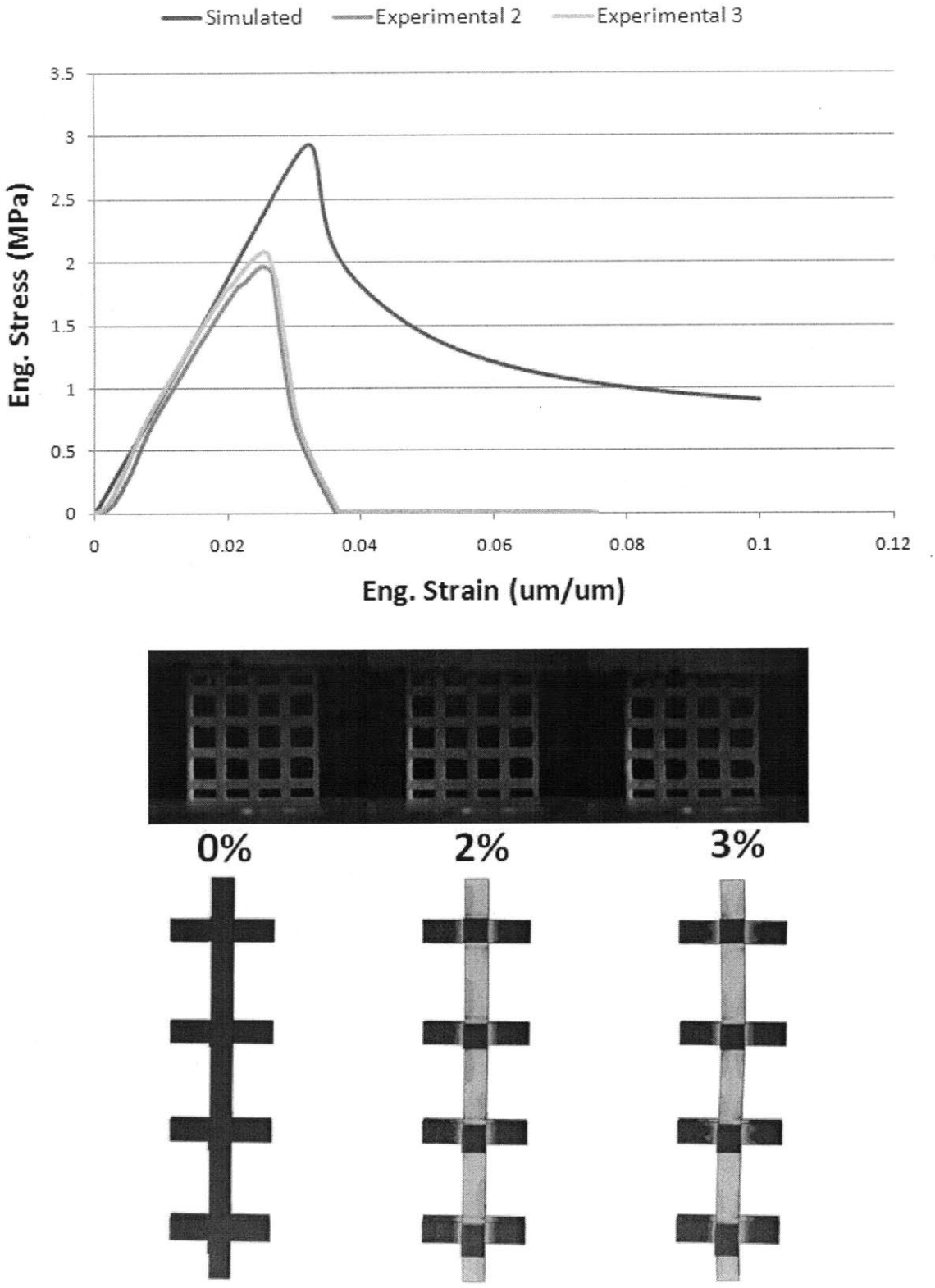

Figure 29: *top* Comparison of simulated and experimental results for a FullCure 720 four-layer structure with a volume fraction of 0.10. *bottom* Test photos and simulation geometry are compared for given strain levels at the initial stage, pre-buckling, post-buckling, and buckled conditions.

4.3.2. Tango Plus

The finite element simulation for the Tango Plus samples correlated well with the experimental results. The simulated modulus and simulated peak stress were very close to actual values. In the case of the volume fraction of 0.20, the simulated modulus was 58 kPa, compared to an experimental modulus of 64 kPa.; for the volume fraction of 0.10, the simulated modulus was 31 kPa, compared to an experimental modulus of 21 kPa. The simulated peak stress for the 0.20 volume fraction was 4.2 kPa , compared to an experimental peak stress of 5.4 kPa; the simulated peak stress for the 0.10 volume fraction was 1.15 kPa, compared to an experimental peak stress of 1.01 kPa. Figures 30 and 31 show the curves. The preload for the Tango Plus samples was 0.5 N, which is a non-trivial amount and necessitated the extrapolation of the beginning of the experimental stress-strain curves for the volume fraction of 0.10 in Figure 20.

Both the modulus and the peak stress for both volume fractions are well-approximated here, and a small discrepancy in the peak stress for the 0.20 volume fraction could be accounted for by imperfections in the printing process. In must be noted that the plateaus in the simulated responses are completely flat, where the experimental samples demonstrate a small softening effect. The finite-element simulation does not account for this softening "peak" in the buckling of elastomeric structures, which occurs due to the method of deformation. However, the initial modulus behavior is well-predicted by this model as verified in a separate study, and the peak is also well captured [25].

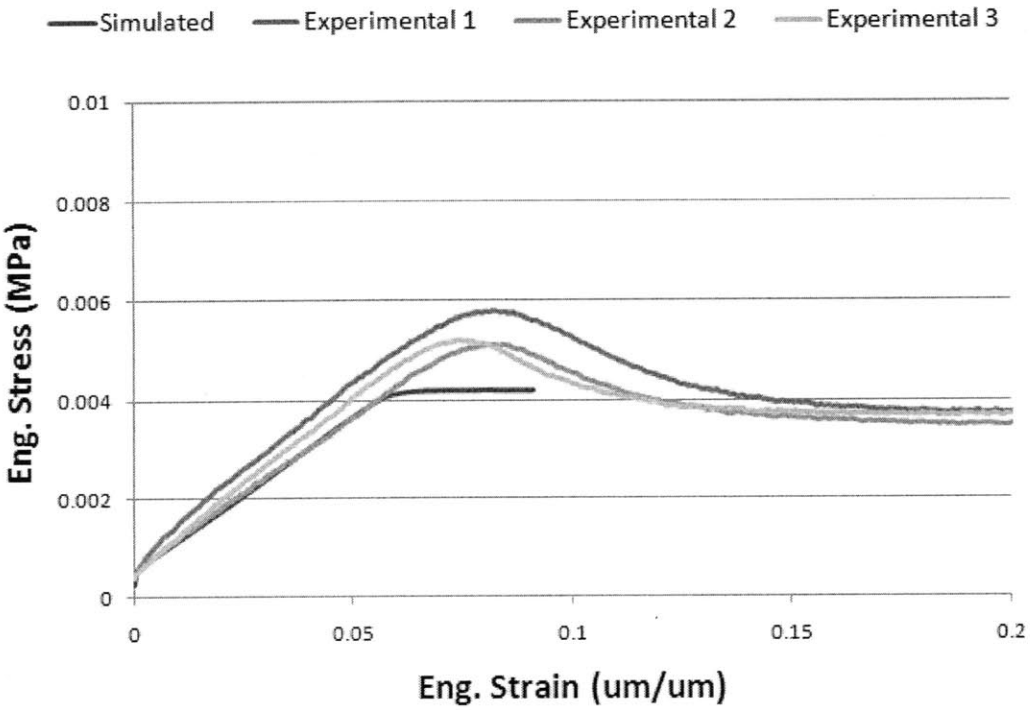

Figure 30: *top* Comparison of simulated and experimental results for a Tango Plus four-layer structure with a volume fraction of 0.20.

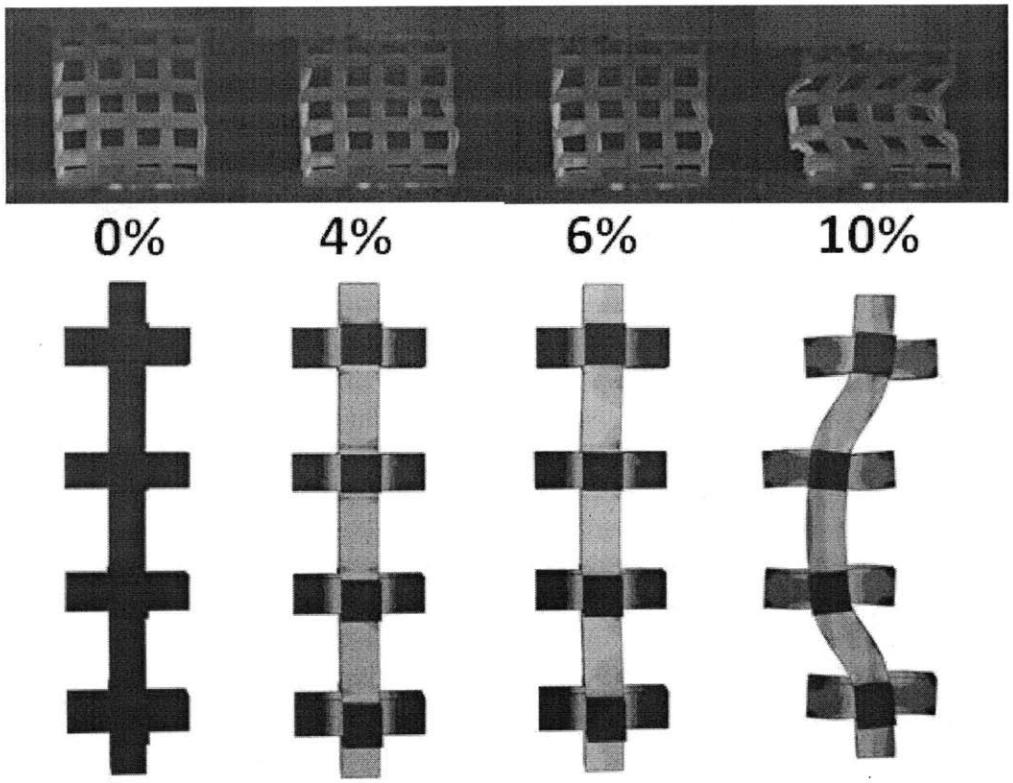

Figure 30 (contd.): *bottom* Test photos and simulation geometry are compared for given strain levels at the initial stage, pre-buckling, post-buckling, and buckled conditions.

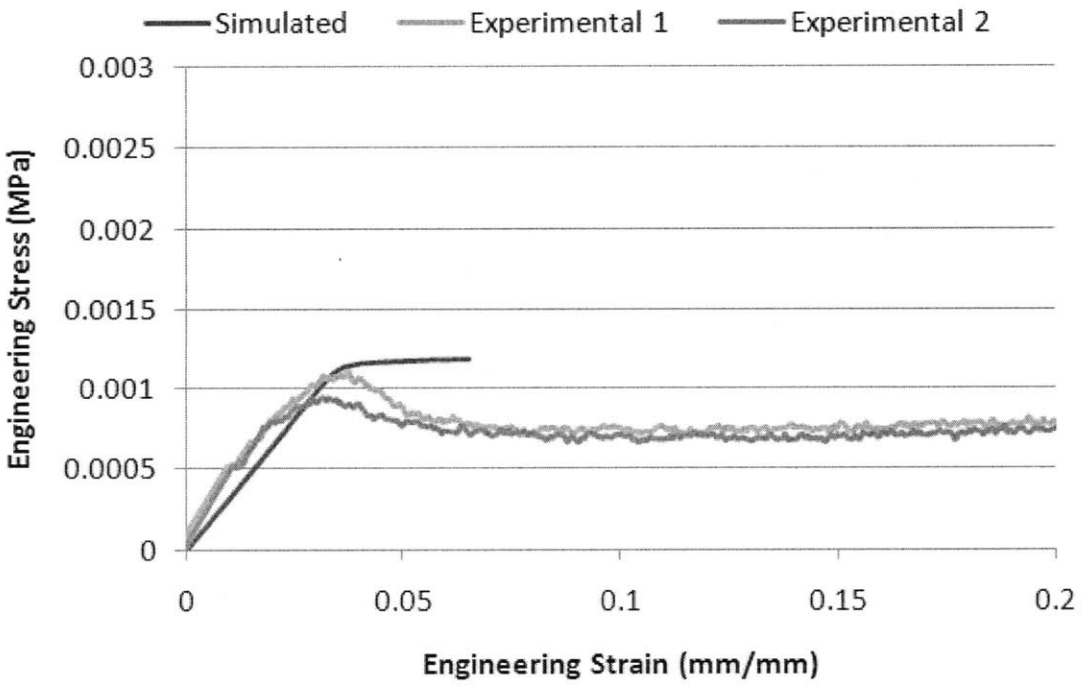

Figure 31: *top* Comparison of simulated and experimental results for a Tango Plus four-layer structure with a volume fraction of 0.10.

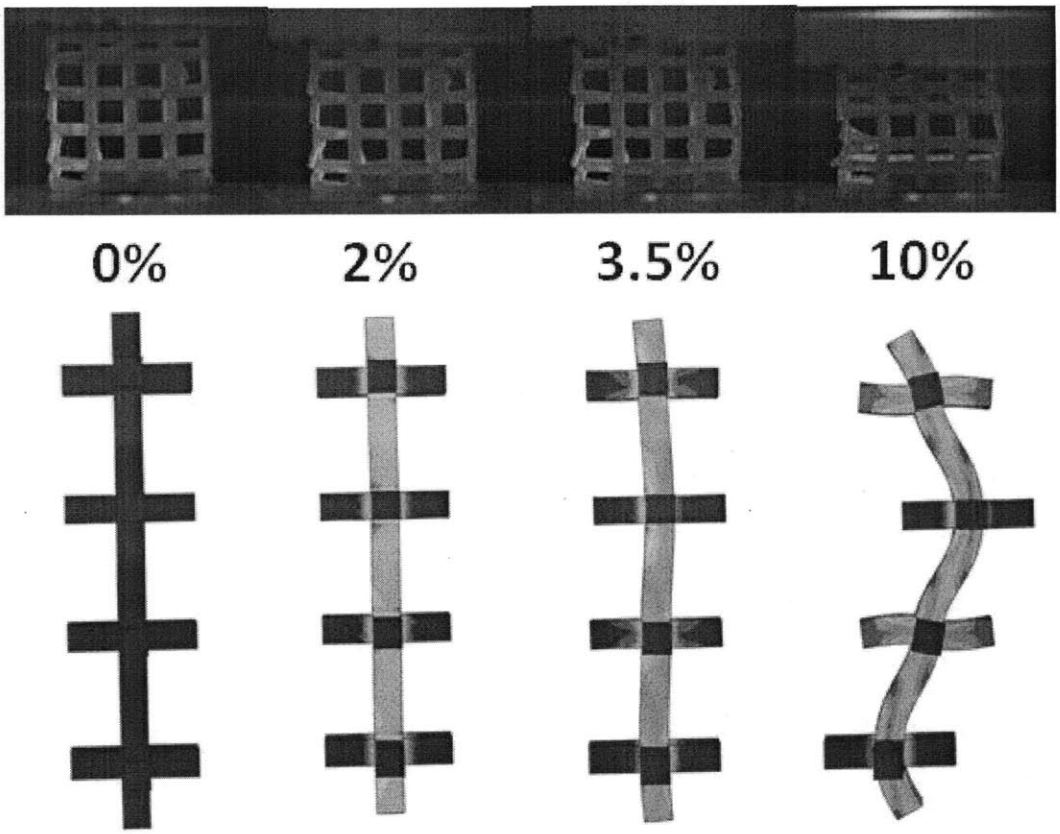

Figure 31 (contd.): *bottom* Test photos and simulation geometry are compared for given strain levels at the initial stage, pre-buckling, post-buckling, and buckled conditions. Both samples tested buckled out of the camera viewing plane, so visual comparison here is difficult.

4.3.3. Composites

Due to the delicate nature of the samples and variations in feature size and strength, the deformation of the composites is not as repeatable as that of the Tango Plus or FullCure 720. The experimental results to not correlate well with the simulations. For the 0.20 volume fraction, the simulated modulus is 75 MPa, as compared to a much smaller 14 MPa experimental modulus; the 0.10 volume fraction shows a similar disparity with a simulated modulus of 44 MPa and an experimental modulus of 9 MPa. The peak stresses are 2.92 MPa and 0.57 MPa for the 0.20 volume fraction simulation and experiment, respectively; the 0.10 volume fraction peak stresses are 1.34 MPa for the simulation and 0.23 MPa for the experiment. Figures 32 and 33 show the stress-strain curves for the composites.

The composite samples experienced the yielding (or fracture) of the outer coating of FullCure 720, and then the characteristic collapse plateau of a foam under compression. As the polymer begins to plastically flow the stress of the RVE peaks and then decreases rapidly as a plastic hinge is formed and collapse ensues.

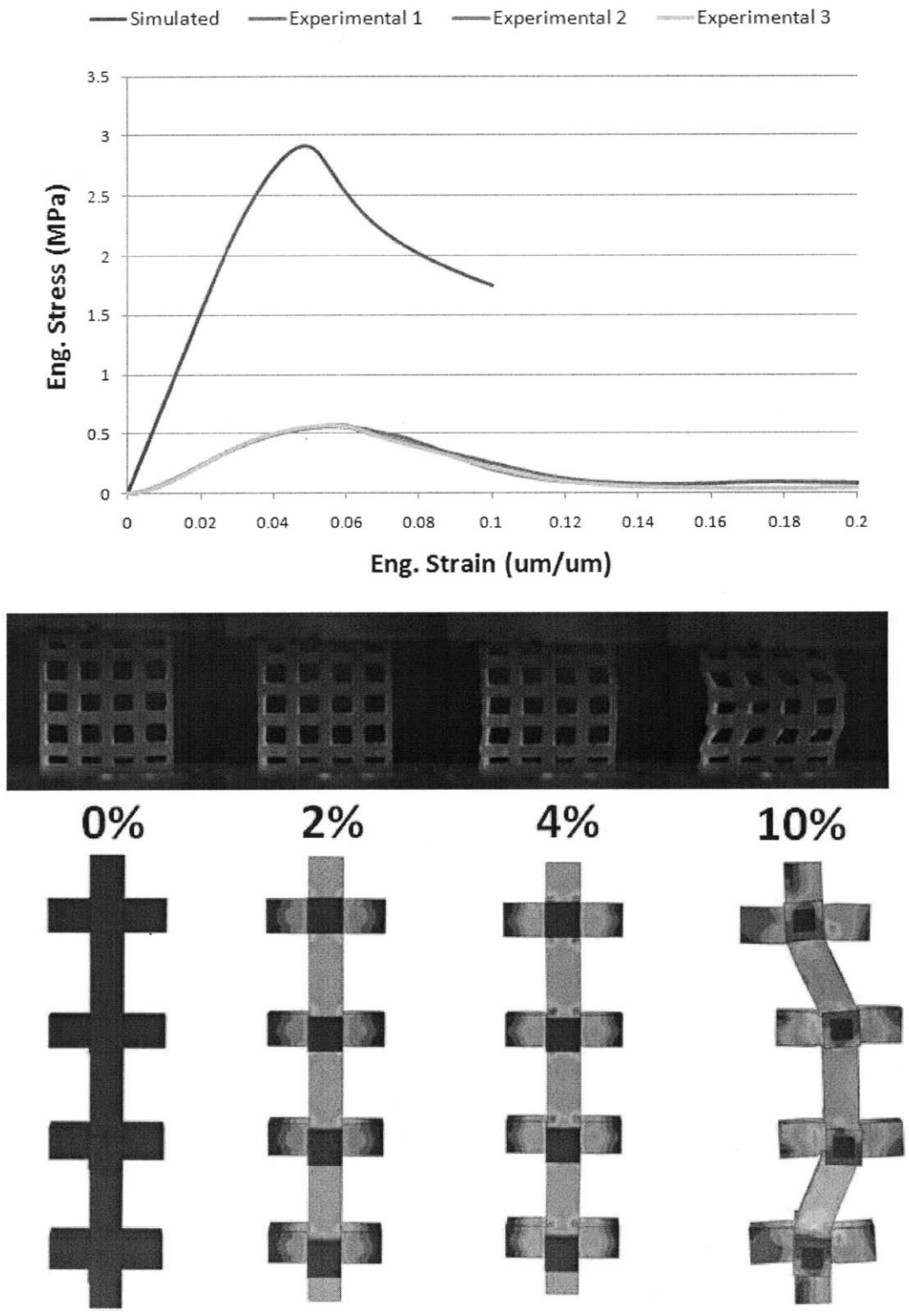

Figure 32: *top* Comparison of simulated and experimental results for a composite four-layer structure with a volume fraction of 0.20. *bottom* Test photos and simulation geometry are compared for given strain levels at the initial stage, pre-buckling, post-buckling, and buckled conditions.

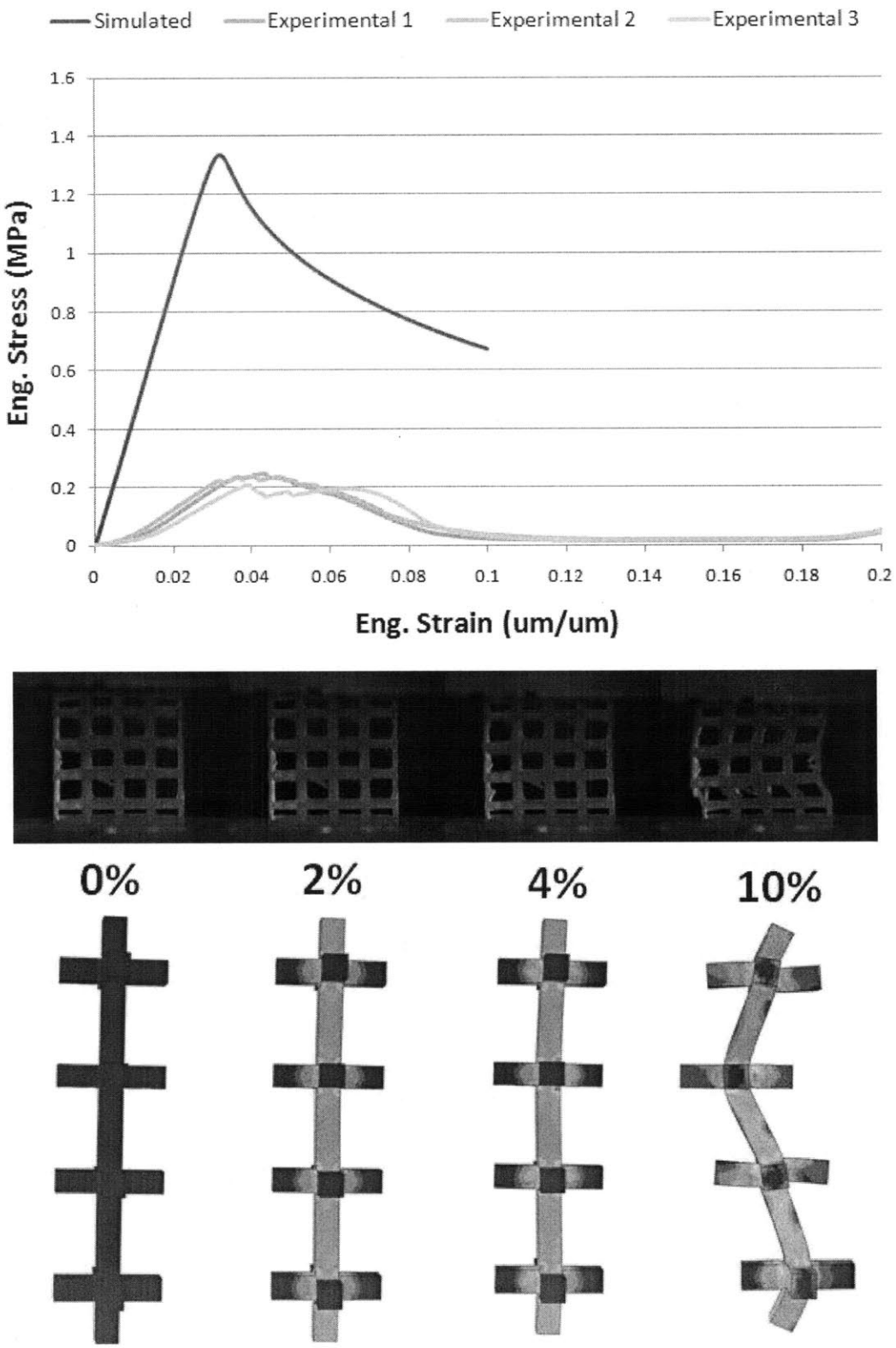

Figure 33: *top* Comparison of simulated and experimental results for a composite four-layer structure with a volume fraction of 0.10. *bottom* Test photos and simulation geometry are compared for given strain levels at the initial stage, pre-buckling, post-buckling, and buckled conditions.

The full stress-strain curves for the composite samples also demonstrate an interesting feature correlated to the geometry of the tested part. Because the failure mode of the composite is column buckling, and because every buckling joint in a real part has a slightly different critical load capacity due to geometric imperfections among other things, each layer of the structure fails consequently rather than concurrently. This deformation mechanism was captured clearly in Figure 34. The first peak represents the primary buckling event; the second corresponds to a secondary buckling event, and the third peak represents the final buckling event before densification begins.

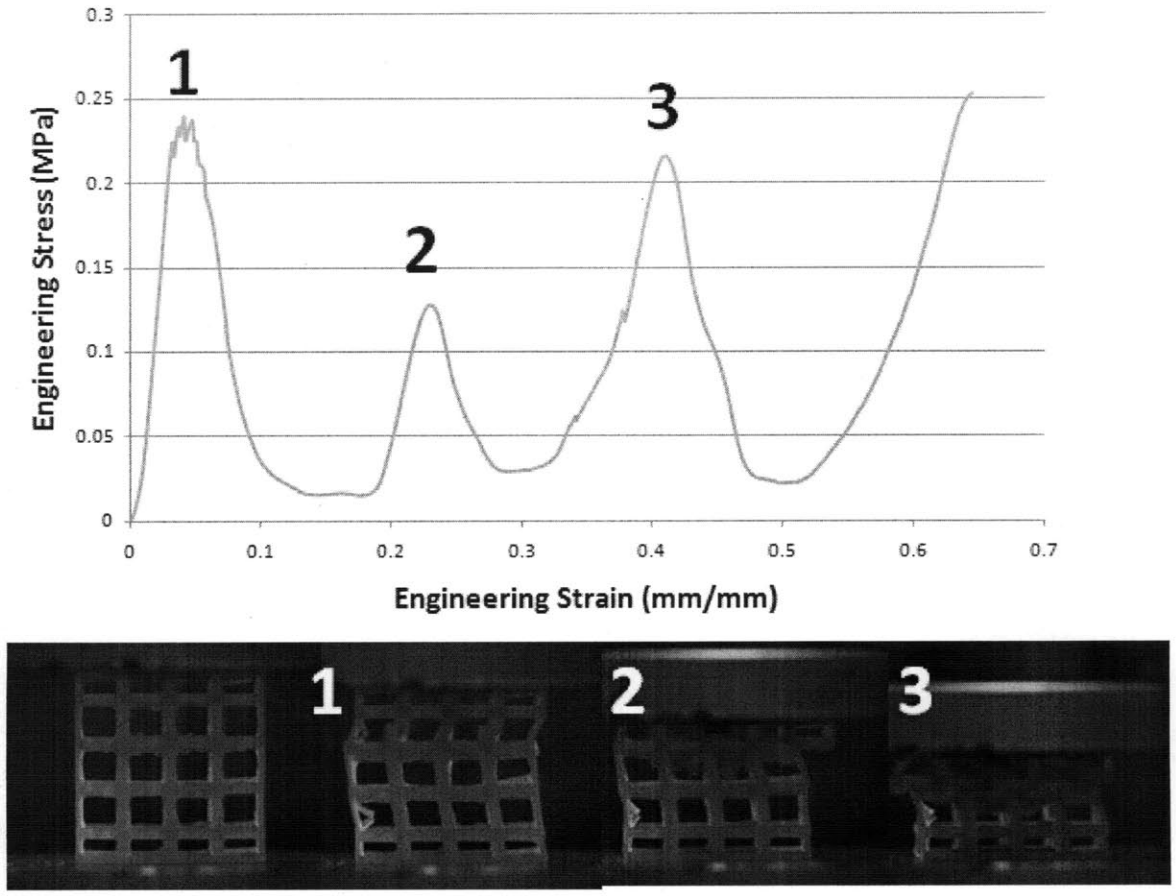

Figure 34: Stress-strain curve for a composite sample with a volume fraction of 0.10 and a coating fraction of 0.20. All three buckling events, corresponding to the three inter-layer struts in the four-layer printed samples, are clearly visible. Densification follows afterward.

One reason for the disparity between the finite-element model and the 3D printed samples likely lies with the FullCure 720 coating. After the test, the six composite samples tested were dissected across the columns and measured under optical magnification to verify the thickness of the coating. The resulting values appear in Table 2. The total volume fraction of the samples was larger than expected; the strut width of each sample was 200-300 μm oversized. However, the modulus and peak stress of the composite are both governed by the stiff polymer coating, so an increase in the core dimensions is of little concern for our parameters of interest. The coating and core both sheared during the dissection, but even so it is apparent that the coating is undersized by 50-150 μm for each sample. The higher volume fraction composite has this problem to a large degree, with two samples' thickness undersized by 150 μm (for a 400 μm

designed value). Because the modulus scales directly with the area of the stiff outer layer, and that area scales to the square of the thickness, a small change in thickness results in a large change in area. The buckling strength of the column is directly proportional to the second moment of area of the outer layer, which scales with the fourth power of the thickness. A small decrease in the thickness therefore generates a large decrease in the buckling strength of the column. Figure 35 shows a microscopic image of a column with measured dimensions.

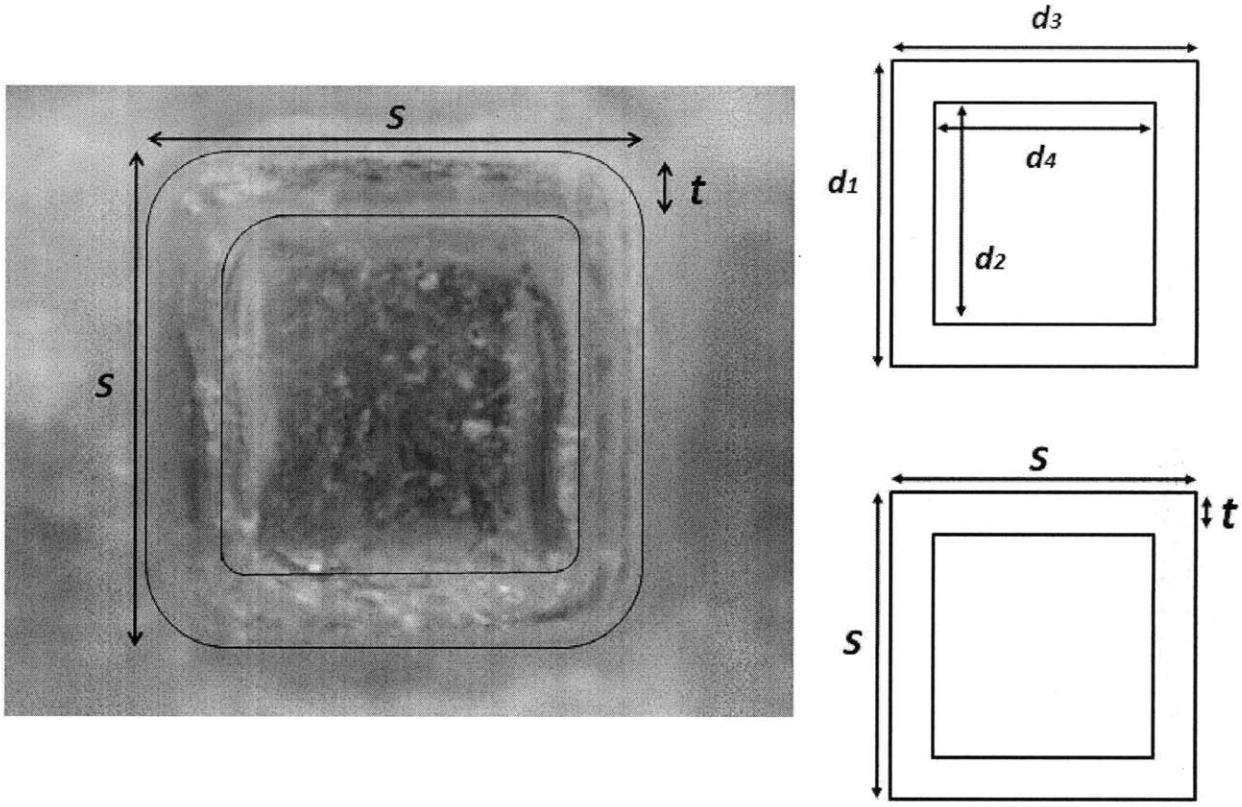

Figure 35: *Left* A closer look at the composition of the composite. The outer layer is the coating; the appearance of another layer on the left and right side-walls is an effect due to the side wall showing through the transparent elastomer and the shearing of both materials during the dissection process. *Right* Reference geometry for measured strut dimensions.

Table 2: Design and measured values for strut dimensions. See the diagram in Figure 35 for reference quantities. All values are in microns.

		d1	d2	d3	d4	(d1-d2)/2	(d3-d4)/2
Composite 1, VF=0.10	*Design*	1500	900	1500	900	300	300
	Measured	1774	1338	1762	1354	218	204
Composite 2, VF=0.10	*Design*	1500	900	1500	900	300	300
	Measured	1782	1289	1758	1313	246.5	222.5
Composite 3, VF=0.10	*Design*	1500	900	1500	900	300	300
	Measured	1807	1248	1750	1256	279.5	247
	VF=0.10 AVG	1787.667	1291.667	1756.667	1307.667	248	224.5
Composite 1, VF=0.20	*Design*	2000	1200	2000	1200	400	400
	Measured	2239	1570	2211	1611	334.5	300
Composite 2, VF=0.20	*Design*	2000	1200	2000	1200	400	400
	Measured	2215	1705	2174	1652	255	261
Composite 3, VF=0.20	*Design*	2000	1200	2000	1200	400	400
	Measured	2174	1660	2227	1701	257	263
	VF=0.20 AVG	2209.333	1645	2204	1654.667	282.1667	274.6667

Based on this hypothesis, further simulation was conducted for the cases of the measured values to verify the experimental results. A simulation was conducted with a strut width of 2200 μm and a coating thickness of 275 μm for the original volume fraction of 0.20. A simulation was conducted with a strut width of 1775 μm and a coating thickness of 225 μm for the original volume fraction of 0.10. The moduli in both cases agree better with the simulated values but are still significantly different. There was a significant decrease in the peak stress during compression for the volume fraction of 0.20, and a smaller decrease in the stress magnitude during compression for the volume fraction of 0.10, corresponding to their respective changes in coating thickness between the original and updated simulations. However, there is still a disparity between the simulated and experimental results, as can be seen in Figures 36 and 37.

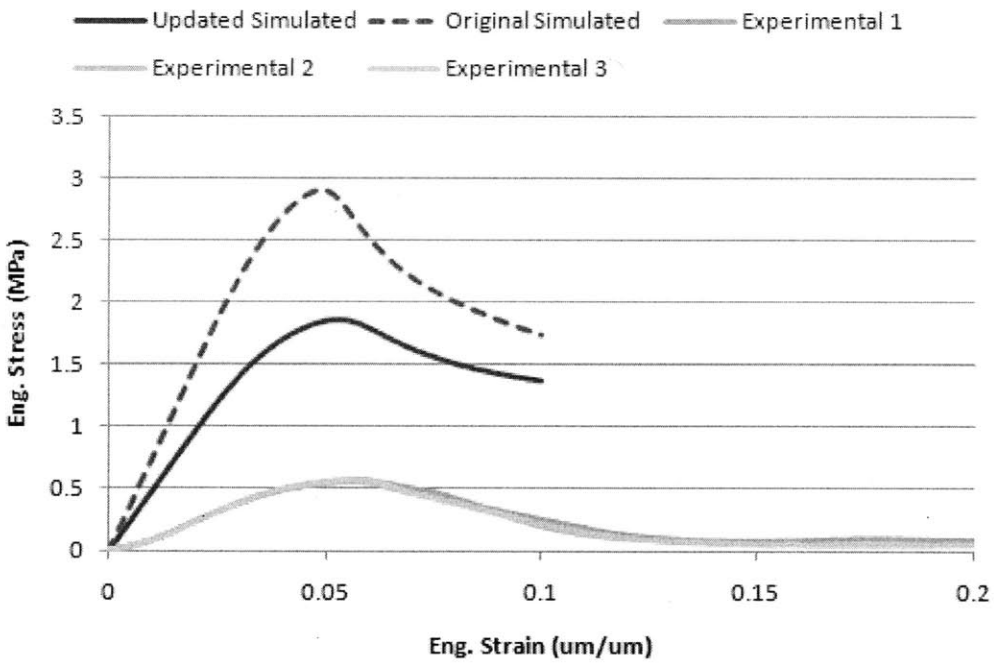

Figure 36: Updated response curve compared to the original simulation and the experimental data for composite structures with a volume fraction of 0.20.

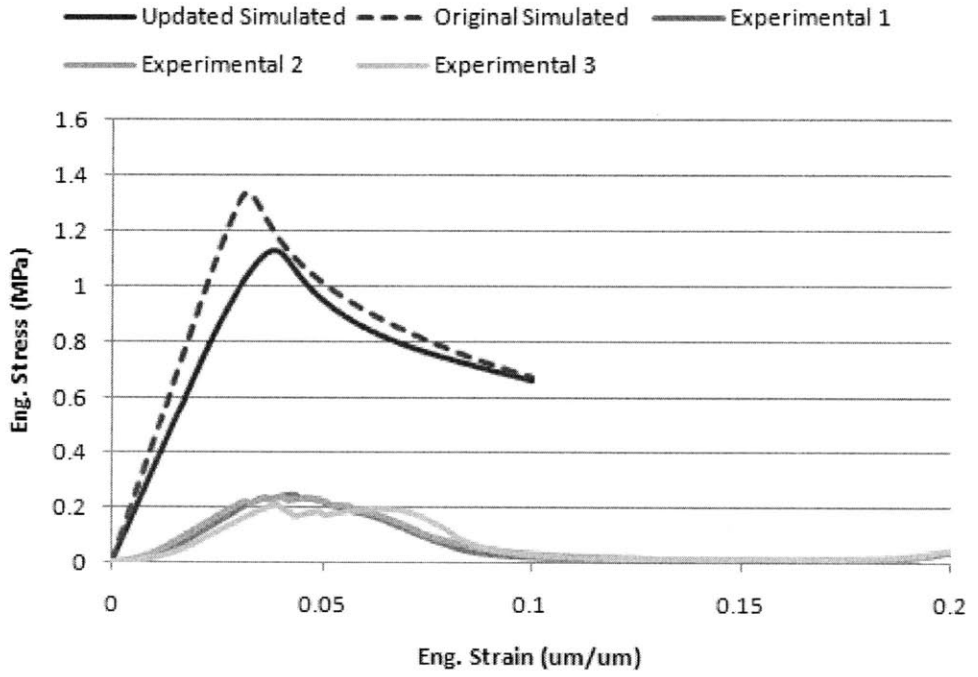

Figure 37: Updated response curve compared to the original simulation and the experimental data for composite structures with a volume fraction of 0.10.

The experimental results show a very low initial modulus for both the volume fractions of 0.20 and 0.10, which then rises to a steady value before decreasing as is expected with increasing strain. This demonstrates that the experimental samples were loaded at a slight angle from the

column axis, and that bending in the struts was present from the very beginning of the experiment. This off-axis loading could partially account for the lack of agreement between the simulated and experimental moduli.

Another discrepancy stems from the printing technology itself. The 3D printing technique used to build the test samples is akin to inkjet printing. The structures are built up vertically and each layer adheres to the next, forming a solid structure when cured. Therefore, the orientation of the part on the printing tray determined the bonding boundaries of the printed material. Materials loaded transversely to the build direction are much more likely to fail prematurely by delamination and the stress concentrations caused by a finite printing resolution. A strut removed from a composite structure is shown in Figure 38. The imperfections on the surface are clear to see, as are the boundaries between the layers of resin.

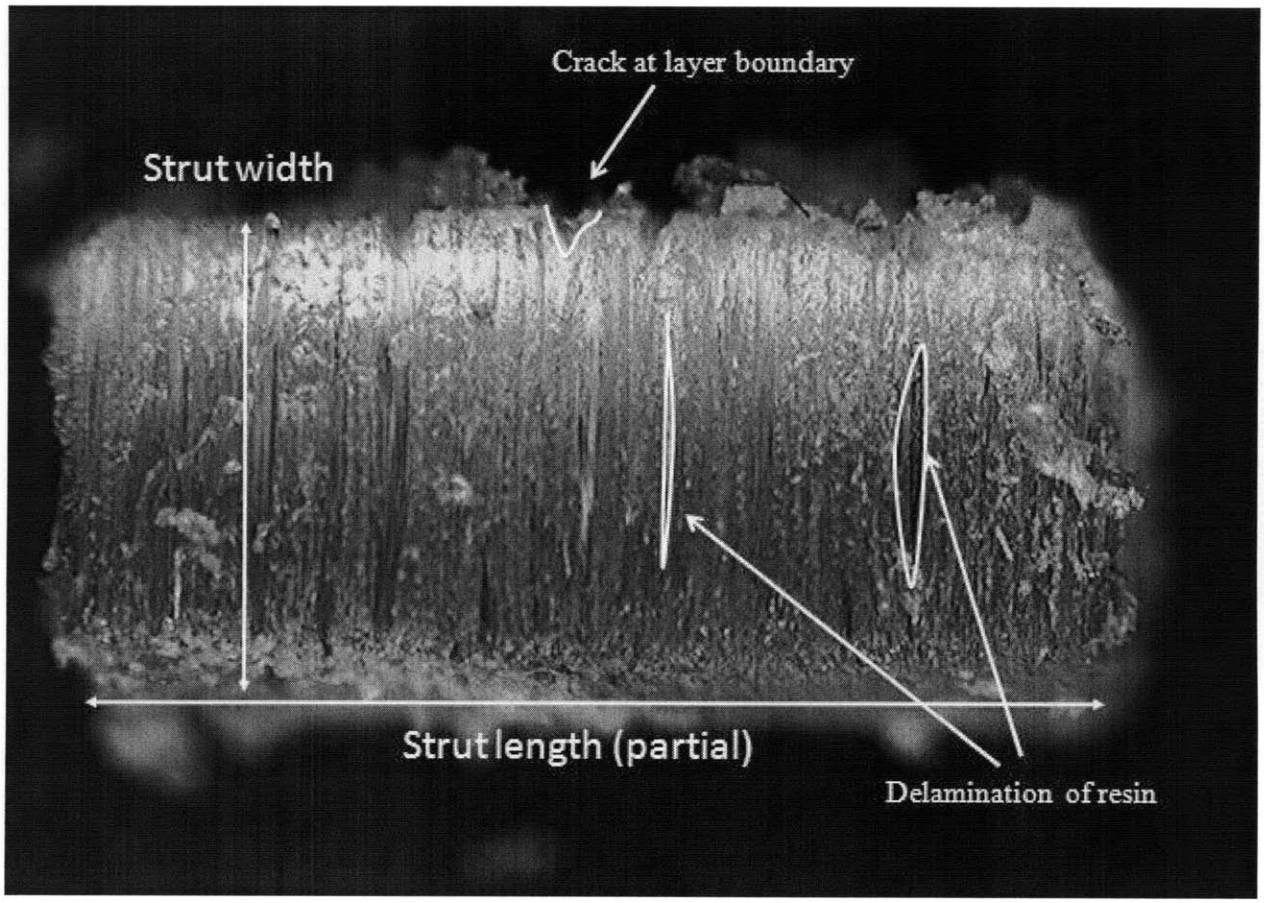

Figure 38: A strut from a composite structure. There are numerous imperfections in the coating surface, and the bonding boundaries between the layers of resin are viewable.

These imperfections can affect the buckling strength of the material since at the site of the imperfection the thickness of the coating is much reduced. We cannot predict the sites of these imperfections, and if they coincide with the deflection points of the buckling mode of the structure, it is very possible that the structure could buckle much earlier than predicted.

Chapter Five: Conclusion

This thesis was a parametric study of the compressive deformation of composite truss-based microstructures. The composite in question was an elastomeric strut coated with a glassy polymer and organized in an open-cellular cubic lattice. Via micromechanical modeling techniques, a finite-element model of a representative volume element was developed and then varied to parametrically consider changes in volume fraction, coating fraction, and layer number. An analytical model was developed to verify the results of the simulation, and experimental samples were fabricated via 3D printing, mechanically tested in compression, and compared to the simulations.

The simulation results exhibited distinct trends. An increase in volume fraction increased the modulus in a linear manner, and increased the peak stress in a non-linear increasing fashion. An increase in the coating fraction significantly increased the modulus; the dependence is nonlinear though it has a linear term that dominates for low volume fractions. The peak stress also has a complex non-linear dependence on the coating fraction that is dominated by a linear term and that causes a significant increase in peak stress for a given increase in the coating fraction. And an increase in the layer number lowered the critical buckling strength of the RVE, which appeared to verge asymptotically with increasing layer number. None of the higher-layer simulations buckled in an ideal mode, which contributed to the small decrease in buckling strength with increasing layer number.

Though the FullCure 720 and Tango Plus experimental samples fit decently with their respective simulations, there was not a great deal of agreement between the experimental results and the simulation for the composite structures. It is possible that this was due to problems with the 3D printed coating on the composite structures, which was both undersized and not continuous, resulting in a far decreased modulus and peak strength as compared to the simulations. However, there is a great deal of promise in this approach if the printing technology can develop to a point where a consistent and repeatable coating may be applied to a structure at micron resolution.

Further work in this vein could include a complete analysis of the energy dissipation techniques in composite trusses, and temperature and strain rate effects on the glassy polymer coating. While foams have a very extensive selection of literature to reference, the realm of composite cellular solids is still a relatively new field, and it is not clear how the classical cellular solid relations may be altered to account for composites of two, three, or even more materials.

It is also possible to consider other material combinations. A stiff glassy polymer and flexible elastomer are a good combination for lightweight energy dissipation, but if a different response is desired, one could combine two polymers with different strain-rate effects, different glass transition temperatures, or use different classes of materials altogether. Ceramics and metals are two such classes not covered here, but each has their own range of very practical uses and a high range of strength.

Micro-scale composites can create a novel range of mechanical response at low weight, and therefore open up a new realm of possibilities for structural and personal protective applications. The study of materials in general is a vital interest to just about every consumer and industrial product, and the emerging trend of micro- and nano-scale manipulation to enhance macroscale results is certainly worth the highest levels of attention. As technology improves over

the next years, such modifications will likely become commonplace, to the benefit of not only academics and materials scientists, but everyone.

References

[1] Gibson, Lorna J., and Ashby, Michael F. *Cellular Solids: Structure & Properties*. New York: Pergamon Press, 1988.

[2] Cheng, Nadia G. "Design and analysis of active fluid-and-cellular solid composites for controllable stiffness robotic elements." Thesis (S.M.), Massachusetts Institute of Technology, Dept. of Mechanical Engineering, 2009.

[3] Gibson, Lorna J., and Ashby, Michael F. *Cellular Solids: Structure & Properties*. New York: Pergamon Press, 1988. pp.3.

[4] Gibson, Lorna J., and Ashby, Michael F. *Cellular Solids: Structure & Properties*. New York: Pergamon Press, 1988. pp. 4.

[5] Gibson, Lorna J., and Ashby, Michael F. *Cellular Solids: Structure & Properties*. New York: Pergamon Press, 1988. pp. 5.

[6] Gibson, Lorna J., and Ashby, Michael F. *Cellular Solids: Structure & Properties*. New York: Pergamon Press, 1988. pp. 31.

[7] Crandall, Stephen H., Dahl, Norman C., and Lardner, Thomas J. *An Introduction to the Mechanics of Solids*. New York: McGraw Hill, 1999.

[8] L. Wang, C. Ortiz, M. Boyce. "Mechanics of Indentation of Nanotube/nanorod Forests." Unpublished (draft), Cambridge, MA.

[9] Brush, Don. O., and Almroth, Bo O. *Buckling of Bars, Plates, and Shells*. New York: McGraw Hill, 1975. pp. 31-37.

[10] Jacobsen, Alan J., Barvosa-Carter, William, and Nutt, Steven. "Compression behavior of micro-scale truss structures formed from self-propagating polymer waveguides." Acta Materialia 55 (2007), 6724-6733.

[11] Maldovan, Martin, Ullal, Chaitanya K., Jang, Ji-Hyun, and Thomas, Edwin L. "Sub-Micrometer Scale Periodic Porous Cellular Structures: Microframs Prepared by Holographic Interference Lithography." Advanced Materials 19 (2007), 3809-3813.

[12] Brush, Don. O., and Almroth, Bo O. *Buckling of Bars, Plates, and Shells*. New York: McGraw Hill, 1975. pp. 11.

[13] Brush, Don. O., and Almroth, Bo O. *Buckling of Bars, Plates, and Shells*. New York: McGraw Hill, 1975. pp. 23.

[14] Objet Geometries Inc. "Objet." <http://www.objet.com/> Accessed May 5, 2010.

[15] Wang, Lifeng. "3D printing for porous structure and polymer composites." Unpublished, Cambridge, MA.

[16] Gibson, Lorna J., and Ashby, Michael F. *Cellular Solids: Structure & Properties*. New York: Pergamon Press, 1988. pp. 122.

[17] Crandall, Stephen H., Dahl, Norman C., and Lardner, Thomas J. *An Introduction to the Mechanics of Solids*. New York: McGraw Hill, 1999. pp. 595

[18] Wang, Lifeng. "3D printing for porous structure and polymer composites." Unpublished, Cambridge, MA.

[19] Timoshenko, S. *Strength of Materials, Part II: Advanced Theory and Problems*. New York: Robert E. Krieger Publishing Company, 1958. pp. 161-165.

[20] Danielsson, M., Parks, D.M., and Boyce, M.C. "Three-dimensional micromechanical modeling of voided polymeric materials." Journal of the Mechanics and Physics of Solids 50 (2002), 351-379.

[21] Wang, Lifeng, Boyce, Mary C., Wen, Cheng-Yen, and Thomas, Edwin L. "Plastic Dissipation Mechanisms in Periodic Microframe-Structured Polymers." Advanced Functional Materials 19 (2009), 1343-1345.

[22] Wang, Lifeng. "Periodic Boundary Condition for Representative Volume Elements." Unpublished, Cambridge, MA, February 28, 2008.

[23] Danielsson, Mats, Parks, David M., and Boyce, Mary C. "Micromechanics, macromechanics and constitutive modeling of the elasto-viscoplastic deformation of rubber-toughened glassy polymers." Journal of the Mechanics and Physics of Solids 55 (2007), 538-539.

[24] Objet Geometries Inc. "Connex500 Multi-Material 3D Printing System." <http://www.objet.com/3D-Printer/Connex500> Accessed March 28, 2010.

[25] Wang, Lifeng. "3D printing for porous structure and polymer composites." Unpublished, Cambridge, MA.